Degree Project in Electrical Engineering, specializing in Systems, Control and Robotics

Second cycle, 30 credits

Modelling of Sloshing Dynamics for AOCS Simulation

FRANCESCA BARBIC

Modelling of Sloshing Dynamics for AOCS Simulation

FRANCESCA BARBIC

Master's Programme, Aerospace Engineering, 120 credits
Date: November 23, 2025

Supervisors: Robin Courson, Pedro Roque
Examiner: Dimos V. Dimarogonas
School of Electrical Engineering and Computer Science
Host company: OHB-Sweden
Swedish title: Modellering av sloschdynamik för AOCS-simulering

Abstract

As space missions impose increasingly strict requirements on spacecraft attitude control and maneuverability, shaping an accurate yet efficient model of propellant sloshing becomes essential. Such model not only support advanced control strategies but also enhance mission safety and reusability. This work adopts a mechanical-equivalent approach that reproduces key physical behavior as effective inertia, slosh modes, and mass displacement, while maintaining computational efficiency. The model is implemented in Simulink for direct integration with the Attitude and Orbit Control System (AOCS).

Firstly, a complete parameter set is derived as a function of fill ratio for representative tanks in both low-g and high-g conditions. Then, a modular structure is introduced, using the Bond number (Bo) as the switching condition between regimes. Three configurations are addressed: stable high-g (Mode 1), stable low-g (Mode 2), and a transitory state (Mode 3), with a mixed regime spanning the transition between capillarity- and gravity-dominated behavior. New formulations for Modes 2 and 3 are developed, and their parameters are characterized. Finally,the coupled interaction between sloshing and spacecraft dynamics is analyzed, and the general model applicable across mission phases, tank geometries, and fluid types is provided.

Keywords

Slosh, Sloshing model, Attitude and orbit control system, spacecraft dynamics coupling.

Abstract

När många rymduppdrag ställer allt högre krav på rymdfarkosters attityd- och manöverkontroll blir det avgörande att utveckla en modell av drivmedelssvängningar i tankar som är både noggrann och beräkningseffektiv. En sådan modell möjliggör inte bara avancerade styrstrategier utan bidrar också till ökad säkerhet och återanvändbarhet. I detta arbete används en mekaniskt ekvivalent metod som återger centrala fysikaliska egenskaper – såsom effektiv tröghet, svängningsmoder och massförskjutning – med bibehållen beräkningseffektivitet. Modellen implementeras i Simulink för direkt integration i Attitude and Orbit Control System (AOCS).

En fullständig parameteruppsättning härleds som funktion av fyllnadsgrad för representativa tankar under både låg-g- och hög-g-förhållanden. Därefter introduceras en modulär struktur där Bond-talet (Bo) används som kriterium för övergång mellan olika regimer. Tre konfigurationer behandlas: stabil hög-g (Mode 1), stabil låg-g (Mode 2) och ett övergångstillstånd (Mode 3), samt ett blandat tillstånd som beskriver skiftet mellan kapillär- och gravitationsdominerat beteende. Nya formuleringar för Mode 2 och Mode 3 utvecklas och deras parametrar bestäms. Slutligen analyseras den kopplade dynamiken mellan svängningar och rymdfarkostens rörelser, och en generell modell presenteras som kan tillämpas på olika uppdragsfaser, tankgeometrier och vätskor.

Nyckelord

Slosh, Sloshingmoder, Attityd- och omloppskontrollsystem, dynamisk koppling.

Acknowledgements

As I am writing the final bits of this thesis, I would like to thank all the people who supported me from the beginning of this project. Firstly, I want to thank my supervisor Robin who always found time to listen and guide me through the work, with support and valuable solutions. To Francesco and the entire AOCS team at OHB, thank you for making me feel welcomed from the very first days. Thanks to my KTH supervisor Pedro and examiner Dimos for accepting with enthusiasm to follow the development of this project and giving guidance and interesting inputs for the analysis.

Of course, it also owns its place on this page, the huge structure of love and support around me that actually made me achieve this. So a really felt *thank you* to the all friends and family here in Stockholm and back in Italy that patiently listened to me for so long. To those with to-do plans, those with long calls and those with food prep. To my number one fan, who always cheered for my success and to whom I owe so much!

Acronyms

AOCS	Attitude and Orbit Control System
CFD	Computational Fluid Dynamics
COM	Center of Mass
DOF	Degree of Freedom
EOM	Equation of Motion
ESA	European Space Agency
FEM	Finite Element Method
ISS	International Space Station
JWST	James Webb Space Telescope
VOF	Volume of Fluid

Contents

Nomenclature

$\mathcal{L}$	Lagrangian
$\mathcal{L}'$	Lagrangian in translating frame
$\mathcal{L}_0$	Lagrangian in inertial frame
ν	Kinematic viscosity (m^2/s)
Ω	Rotating frame angular velocity (rad/s)
ω	Angular velocity (rad/s)
Φ	Velocity Potential (m^s/s)
σ	Surface tension (N/m)
θ_c	Contact angle (deg)
ζ	Damping ratio
A	Surface area (m^2)
a	Acceleration (m/s^2)
Bo	Bond number
d	Tank diameter (m)
E	Energy (J)
E_0	Energy in inertial frame (J)
E_k	Kinetic energy (J)
f_n	Natural frequency (Hz)
Fr	Froud number

g	Gravitational acceleration (m/s^2)
h	Fluid height (m)
h	Tank height (m)
h_0	Static mass displacement (m)
h_i	ith-Hinge point distance (m)
h_{fluid}	Fluid height in the tank (m)
k	Spring stiffness (N/m)
k_{eff}	Equivalent spring constant (N/m)
L_i	ith-Pendulum rod lenght (m)
l_i	Distance of mass i from free surface (m)
M	Angular momentum (kg·m^2/s)
m	Mass (kg)
M_0	Angular momentum in inertial frame (kg·m^2/s)
m_0	Static mass (kg)
m_i	Sloshing masses (kg)
m_T	Total mass (kg)
p	Linear momentum (kg·m/s)
p_0	Linear momentum in inertial frame (kg·m/s)
U	Potential energy (J)
v'	Translating frame velocity (m/s)
v_0	Velocity in inertial frame (m/s)
V_n	Normal component of velocity (m/s)
V_{tank}	Tank volume (m^3)
w	Tank width (m)
We	Weber number

x_0 Time-varying displacement (m)

Chapter 1

Introduction

This thesis addresses the development of a Simulink model to represent the sloshing phenomenon. In general, the term sloshing refers to the oscillatory motion of a liquid inside a container when subjected to external accelerations or rotational dynamics. Understanding this behavior is essential in both terrestrial and space applications, though the associated risks and operational requirements differ significantly.

As for terrestrial context, an example of sloshing can be found on trucks transporting liquids in large containers mounted along the length of the vehicle itself. The motion of the liquid is influenced by road irregularities, such as bumps or sudden turns, which can shift the truck's centre of mass in unpredictable ways, increasing the risk of rollover or loss of maneuverability. Space applications involve instead some further complexity. On Earth, gravity provides a constant stabilising acceleration that governs fluid motion. In space, however, objects experience conditions of near weightlessness because they are in continuous free fall around Earth. During a space mission, both the magnitude and direction of accelerations and rotations can vary significantly across different flight phases. Conditions range from the high accelerations experienced during launch, to prolonged periods of microgravity when the spacecraft is in a quiescent or idle state. This variability creates many possible configurations and motion that the fluid would follow, all of which need to be tracked and studied to maintain performance and to ensure mission safety.

In a spacecraft, the subsystem most affected by sloshing dynamics is Attitude and Orbit Control System (AOCS). This subsystem is responsible for controlling and maneuvering the spacecraft, which requires precise tracking of the inertia distribution

in all configurations, as well as accurate knowledge of both the static and dynamic Center of Mass (COM). As the name suggests, the dynamic component of the COM is influenced by all motion within the spacecraft. This includes the deployment or movement of solar panels or booms, optical equipment pointing maneuvers, and, importantly, the movement of propellant inside the tanks.

Accurate knowledge of how the fluid moves and settles is a significant advantage for spacecraft control using reaction wheels and thrusters. If the motion of the fluid is not represented in the AOCS algorithm, it becomes an unmodelled disturbance in the control loop. While control systems are often designed to be robust to such disturbances, performance and accuracy improve significantly when the control algorithm accounts for the actual motion in advance. The pointing accuracy requirements for many modern satellites and spacecraft have risen to extremely high standards in recent missions. Earth observation satellites such as Sentinel-2 require angular stability in the order on 10^{-6} rad for submeter image resolution [21]. For astronomy missions, like James Webb Space Telescope (JWST), it can demand stability below 7 milliarcseconds to keep images non blurred after long exposure[20]. But these is also true for communication satellites, especially when they present high data-rate. Such levels of precision leave very little tolerance for unmodelled disturbances such as propellant sloshing, especially during critical maneuvers or fine pointing phases.

Sloshing analysis therefore becomes an essential consideration in the design of control algorithms for missions requiring high precision. The present work investigates previously used modelling approaches through a literature review and develops a suitable model for the various phases of a typical space mission. This model is designed with consideration of general space environment characteristics, required manoeuvres, common tank geometries, and typical interfaces between the sloshing model and other components of the AOCS algorithm.

1.1 Motivation

The motion of fluid in spacecraft tanks can represent a significant fraction of the total spacecraft mass moving in an uncontrolled manner during each phase of a mission. This not only affects the geometric and mass properties of the system but also poses direct risks to mission safety. Uncontrolled fluid motion can

compromise spacecraft maneuverability, potentially overwhelming the capabilities of AOCS hardware, including reaction wheels and thrusters. Moreover, resonance between the fluid motion and the spacecraft's structural or control system frequencies could lead to catastrophic build-up, ultimately causing mission failure.

As modern missions impose increasingly tight performance requirements, the allowable margin for unmodeled disturbances becomes minimal. Accurate knowledge of all spacecraft subsystems is essential to ensure maximal performance. This is particularly critical for high-precision pointing and proximity operations. For instance, the European Space Agency (ESA) Comet Interceptor mission aims first to detect and select a comet based on in-orbit observations. After handling precise thrusting maneuvers at relatively high accelerations, the spacecraft will have to accurate point its instruments towards a comet. This is required to be performed in high accuracy while in microgravity conditions. The conditions of the encounter are considered to be possibly inducing some transitory motion in the tank due to impact of dust and precise impulses.

Experimental studies of fluid motion, such as those conducted on the International Space Station (ISS), provide insights into the fundamental behavior of fluids in microgravity aimed to a scientific undestanding of the phenomenon but with no practical solution or uses. Meanwhile, other investigations are based on computationally intensive methods to simulate fluid dynamics under various conditions. In aeronautics, fluid dynamics in containers has been extensively studied using both analytical approaches and Computational Fluid Dynamics (CFD) simulations. One commonly used technique for sloshing studies is the Volume of Fluid (VOF) method, which allows precise tracking of the fluid surface deformation. Compared to simpler methods (e.g., potential flow or shallow-water approximations), VOF provides more accurate predictions of spatial distribution, forces exerted on tank walls, and fluid shape under dynamic excitation. All these parameters are indeed highly important for a control environment on a spacecraft.

However, while CFD provides high-fidelity results, it is too computationally expensive to integrate directly into AOCS simulations. Therefore, sufficiently accurate models which also maintain light computational costs are required for real-time control applications. Traditionally, passive control techniques, such as baffles or bladders, have been used to mitigate sloshing. Actively controlling sloshing, however, could

eliminate the need for internal hardware, reducing spacecraft mass, cost, and manufacturing complexity. An accurate sloshing model offers a strategic advantage for spacecraft manufacturers by enhancing safety, reliability, and overall mission performance while reducing both operational and environmental risks. It is worth noting that detailed knowledge of how AOCS systems handle sloshing is rarely public, making research in this area both more challenging and especially needed. Apart from technical performance, the usage of passive hardware has impact on budget and sustainability due to lack of reusability and manufacturing demands. Missions where sloshing is not properly modeled pose safety risks to the spacecraft and payload, potentially causing mission failure or environmental contamination. Accurate, reusable, and actively controllable sloshing models help ensure mission success while reducing environmental impact.

From an industrial perspective, the sloshing model must be computationally efficient, easy to use, and adaptable to various spacecraft designs. Following a modular structure ensures reusability across projects without major redesigns, facilitating integration with other subsystems and enabling future controller development.

1.2 Problem Statement

The real added value of this thesis lies in addressing the gap between scientific and demonstrative experiments, CFD simulations, and linearised analytical models. Current knowledge about sloshing, as presented in publicly available literature, is often not structured in a way that is suitable or convenient for application within an AOCS environment. Existing works have largely focused on specific experimental tanks or setups, without developing a generalised model that can adapt to different tank geometries, fluids, and external conditions. Such generality is essential to ensure reusability across a variety of applications.

Furthermore, current approaches either demand significant computational resources—making them unsuitable for fast, system-level analysis—or oversimplify the physics, reducing their representativeness of real behaviour, especially in the case of large-amplitude oscillations. A physically justified, computationally efficient model capable of representing a wide range of motion types is still lacking.

In addition, industry requirements are rarely integrated into academic research on

this topic. This work addresses that gap by developing a generalised sloshing model that not only incorporates physical accuracy and computational efficiency but is also designed for full integration into the existing simulation environment at OHB. The ultimate goal is to deliver a model that is reusable, physically sound, and directly applicable in industrial contexts.

1.3 Outline

The following chapters present the outcomes of this work in a structured manner. Chapter 2 introduces the theoretical background and the methodology used for the derivations that follow. Chapter 3 builds on the existing literature to justify the mechanical equivalent method and highlight its advantages, while also presenting the models used in this thesis along with their physical foundations. Chapter 4 details the equations derived to describe the different modes, their parameters, and the associated switching logic. Chapter 5 presents the structures and the inputs of the used Simulink model with inputs for its verification. Finally, Chapter 6 discusses the conclusions drawn from this work and reflects on its achievements, while also outlining directions for future research.

Chapter 2

Theoretical Background

This chapter gathers the essential theoretical explanations that, in later chapters, may be assumed as known. Presenting them here ensures the reader has a clear reference point.

The subject of this thesis draws on knowledge from multiple fields: fluid dynamics, control theory, modelling, and analytical mechanics, as well as structural dynamics for understanding natural frequencies. It also requires familiarity with aspects of space missions, including the hardware used for manoeuvring and the various environments a spacecraft may encounter during its mission.

While it is assumed that the reader is already familiar with most of these topics, brief overviews and reminders are provided here to establish a common foundation.

2.1 Resonant Frequency and Structural Dynamics

Every mechanical system has natural frequencies at which it tends to oscillate when disturbed. These resonant frequencies depend on the system's mass distribution and stiffness. For simple systems as single Degree of Freedom (DOF) oscillation mass, the natural frequency is simply derived from $f_n = \frac{1}{2\pi}\sqrt{\frac{k}{m}}$, with k being the stiffness and m the mass of the oscillating body. While for more complex and compound systems as spacecraft, analytical methods like Finite Element Method (FEM) can be used, or alternatively vibration tests are common on space components but not as easily accessible. These ways both deliver the set of natural frequencies and corresponding mode shapes which characterise the specific body.

When an external excitation is applied to a system with near natural frequency, resonance can happen. Indeed, oscillations can be significantly amplified to the limit of becoming a structural risk. In spacecraft, structural resonances can couple with other dynamic phenomena, such as fuel sloshing or flexible appendages oscillations, potentially leading to large attitude disturbances or even control instability. For tanks containing liquid propellant, the sloshing motion has its own set of natural frequencies, often computed using analytical approximations or CFD simulations for more complex cases.

It is important to model these oscillations, which can also change in range under different external conditions. This is relevant not only for structural safety,that however is usually out of danger because of the different ranges in natural frequencies for structure and fluid sloshing; but also because resonance can occur with control system frequencies. This fluid-control interaction can amplify oscillations, degrade pointing accuracy, and in some cases lead to instability if not properly accounted for in the design.

2.2 AOCS Hardware

It is valuable to review the types of control hardware present on a spacecraft, as the outputs of these devices are the main inputs driving the motion of the fluid. To maneuver a spacecraft in the classic six degrees of freedom (three rotations and three translations), reaction wheels and thrusters are typically employed. The number of these components may vary between spacecraft and redundancy is typically maintained.

Reaction wheels are momentum exchange devices used to control a spacecraft's attitude without consuming propellant. Each unit consists of a flywheel driven by an electric motor; by changing the wheel's rotational speed, the spacecraft's body rotates in the opposite direction due to conservation of angular momentum. Reaction wheels enable precise, continuous control and are commonly used for fine pointing in applications such as Earth observation or astronomical missions. Their main limitations are restricted torque capability and the potential for saturation over time if external torques (e.g., from gravity gradients or solar radiation pressure) are not counteracted.

Thrusters provide direct force and torque by expelling mass at high velocity, in accordance with Newton's third law. Depending on mission requirements, they may use chemical propulsion or electric propulsion. Within the AOCS framework, thrusters are often employed for fast attitude maneuvers, reaction wheel de-saturation, or as backup attitude control devices when reaction wheels are insufficient or unavailable. Unlike reaction wheels, thrusters consume propellant, making their use a key factor in mission lifetime management.

2.3 Landau Derivation for Moving Frame

The motion of the fluid in the tank must be described by Equation of Motion (EOM) that provide all relevant information about the fluid mass position and its evolution over time. In this thesis, the EOMs are derived using the Lagrange formalism, which is particularly useful for tracking the evolution of the (DOFs) even in complex, coupled systems. Moreover, the Lagrangian approach offers direct insight into the system's energy balance, which can serve as a valuable tool for assessing the physical reliability of results. Monitoring the evolution of the system's energy and its conservation in the right configurations can be implemented in the model as a tool to check validity.

For this reason, the Landau formalism for deriving equations of motion in a non-inertial frame is presented here, along with its impact on the energy terms. The non-inertial frame is especially relevant for this work, as the spacecraft environment involves both acceleration and rotation. This contrasts with most experimental setups found in the literature, which are typically conducted on stationary tables in laboratory conditions and do not present the coupling effects and non-inertial forces that are present in an actual spacecraft.

It will be considered a moving frame, in particular one which is accelerating with acceleration a and rotating with angular velocity ω , with respect to an inertial frame. In the inertial frame, the Lagrangian is

$$\mathcal{L}_0 = \frac{1}{2} m v_0^2 - U \tag{2.1}$$

and the equation of motion derived from it is

$$m \frac{dv_0}{dt} = -\frac{\partial U}{\partial r} \tag{2.2}$$

Because $\frac{\partial \mathcal{L}_0}{\partial v} = mv_0$ and that derived in time is $\frac{mdv_0}{dt}$ while the Lagrangian partially derived for the position vector is $\frac{\partial \mathcal{L}}{\partial r} = -\frac{\partial v}{\partial r}$.

If the equations of motion are instead derived in a non-inertial reference frame, the Lagrangian is still

$$\frac{d}{dt}\left(\frac{\partial \mathcal{L}}{\partial v}\right) = \frac{\partial \mathcal{L}}{\partial r} \tag{2.3}$$

because it is based on the least action principle which is independent of the frame. However, the transformation $\mathcal{L}_0 \rightarrow \mathcal{L}$ must be defined. It can be considered a process in two steps, defining first a translating frame K', characterised by moving with a velocity $V(t)$ relative to the frame K_0, such as

$$v_0 = v' + V(t) \tag{2.4}$$

Substituting this expression in $\mathcal{L}$, it gives

$$\mathcal{L}' = \frac{1}{2}m(v'^2 + V(t)^2 + 2v'V(t)) \tag{2.5}$$

The second term in the summatory can be omitted if the focus is on the motion of the accelerated frame only, since it can be substituted with a function of time in some other parameter in frame K'. Considering $v' = \frac{dr'}{dt}$ the last term can be expanded in

$$mv'V = mV \cdot \frac{dr'}{dt} = m\frac{d}{dt}(V \cdot r') - m\frac{dV}{dt} \cdot r' \tag{2.6}$$

that when is substituted in $\mathcal{L}'$ results as

$$\mathcal{L}' = \frac{1}{2}mv'^2 - m\frac{dV}{dt}r' - U \tag{2.7}$$

where $\frac{dV}{dt} = a(t)$ is the translational acceleration of the frame K'. In the Lagrangian derived in K', one extra term appears, compared to the inertial frame:

$$m\frac{dv'}{dt} = -\frac{\partial U}{\partial r} - ma(t) \tag{2.8}$$

This means that the equations deriving from the last expression are equivalent to those for the motion of a particle inserted in an homogeneous force field, equal in magnitude to the mass of the particle (m) multiplied by the acceleration a but with opposite sign.

Considering now the transition $K' \rightarrow K$, where K is a rotating frame with angular velocity $\Omega(t)$ relative to K'. The velocity is now expressed as follows

$$v' = v + \Omega \times r \tag{2.9}$$

and, when substituted in $\mathcal{L}_0$, gives the relative Lagrangian $\mathcal{L}$

$$\mathcal{L} = \frac{1}{2}m(v^2 + 2v \cdot \Omega \times r + (\Omega \times r)^2) - U - ma \cdot r \tag{2.10}$$

which represents the Lagrangian in an arbitrary - potentially not inertial - frame.

Also it can be rearranged $mv \cdot \Omega \times dr = mdr \cdot v \times \Omega$ and the Lagrangian differential becomes

$$d\mathcal{L} = mdv \cdot v + mdv \cdot \Omega \times r + mv \cdot \Omega \times dr + m(\Omega \times r) \cdot (\Omega \times dr) - \frac{\partial U}{\partial r} \cdot dr - ma \cdot dr \tag{2.11}$$

The components to derive the governing equations are derived as

$$\frac{\partial \mathcal{L}}{\partial v} = mv + m(\Omega \times r) \tag{2.12}$$

$$\frac{\partial \mathcal{L}}{\partial r} = mv \times \Omega + m(\Omega \times r) \times \Omega - \frac{\partial U}{\partial r} - ma \tag{2.13}$$

and combining in $\frac{d}{dt}\left(\frac{\partial \mathcal{L}}{\partial v}\right) - \frac{\partial \mathcal{L}}{\partial r} = 0$, it results as:

$$m\frac{dv}{dt} = \underbrace{2mv \times \Omega}_{\text{A}} - \underbrace{m\dot{\Omega} \times r}_{\text{B}} - \underbrace{m\Omega \times (\Omega \times r)}_{\text{C}} - \frac{\partial U}{\partial r} - \underbrace{ma}_{\text{D}} \tag{2.14}$$

It is valuable to notice that the labeled terms represent particular pseudo-forces in the non inertial frame:

- A term: Coriolis force, linear term in velocity derived by the rotation of the frame on a moving particle, perpendicular to its motion.
- B term: Euler force, present in frames characterised by varying angular velocity.
- C term: Centrifugal force, it acts perpendicular to the rotation axis and to the position vector, pushing the particle out of the curved trajectory.

- D term: translational force, it has the same magnitude but different direction than a force applied to the frame with same acceleration.

All these forces are present due to the non-inertial nature of the frame considered, the body frame. The the motion of the frame, even if they are not forces directly applied to the internal model, affect the relative equations of motion.

To define the evolution of the single degrees of freedom, when Lagrangian are used, it is needed to complete the derivation in a scalar way, starting from the vectorial Lagrangian in 2.3. For each of the degrees of freedom there is one describing equation, coupled with others degrees of freedom. To compute resulting force can be necessary to shape the position vector deriving from one or more DOF.

2.3.1 Energy Evaluation Moving Frame

When considering the energy stored of the system in the accelerated frame, part of the potential energy associated with the pseudo-potential energy as $-ma$, that acts as a gravity potential in the body frame, actually appears within the kinetic energy expression, as it contributes to the velocity of the mass. In the same way, the so-called centrifugal potential energy introduces additional terms directly into the kinetic energy E_k. The only terms which remain 'proper' potentials are the elastic/surface/thermal potential energy and the gravitational field influence on the mass, even though its magnitude may be very small. However, in a non-inertial frame, the total energy is no longer a constant of motion as it is in an inertial reference frame. While in the inertial frame K_0 the condition $\frac{dE_0}{dt} = 0$ holds in absence of dissipation,for the energy expressed in the non-inertial frame $E(K)$ a more detailed analysis is required.

To evaluate the energy and its change between frames it is convenient to take into consideration as not inertial frame, a frame rotating with constant angular velocity $\Omega = \text{const}$ and with no translational acceleration, to ease the computation without reducing the validity of the results.

For this case, the Lagrangian in 2.3 simplifies to

$$\mathcal{L} = \frac{1}{2}mv^2 + mv \cdot \Omega \times r + \frac{1}{2}m(\Omega \times r)^2 - U \tag{2.15}$$

and the derived equation of motion is

$$m\frac{dv}{dt} = 2mv \times \Omega + m\Omega \times (r \times \Omega) - \frac{\partial U}{\partial r} \tag{2.16}$$

While, when considering energy,it can be derived from the linear momentum as $E = p \cdot v - \mathcal{L}$ where the linear momentum p is

$$\rightarrow \frac{\partial \mathcal{L}}{\partial v} = mv + m\omega \times r \tag{2.17}$$

Hence the energy is expressed as

$$\begin{aligned} E &= mv^2 + mv \cdot \Omega \times r - \frac{1}{2}mv^2 - mv \cdot \Omega \times r - \frac{1}{2}m(\Omega \times r)^2 + U \\ &= \frac{1}{2}mv^2 - \frac{1}{2}m(\Omega \times r)^2 + U \end{aligned} \tag{2.18}$$

The second term of this expression is added due to the rotation of the frame and it is a contribution of centrifugal potential energy. The velocity of a particle in frame K is $v_0 = v + \Omega \times r$, and the linear momentum becomes

$$p = mv + m \cdot \Omega \times r \tag{2.19}$$

$$p_0 = mv + \Omega \times r = mv_0 \tag{2.20}$$

The linear momentum remains constant in different frames $p_0(K_0) = p(K)$. When considering the angular momentum the derivation brings to an equivalent result

$$M_0 = r \times p_0 \tag{2.21}$$

$$M = r \times p \tag{2.22}$$

$$\Rightarrow M_0 = M \tag{2.23}$$

However, it is important to underline that $E_0 \neq E$, therefore it is not possible to use the energy conservation as indicator of physical correctness, because in a non inertial frame, even without dissipative terms, the energy is not constant. In particular, considering 2.18, and substituting in it $v = v_0 - \Omega \times r$ the new expression of the energy

in frame K is

$$\begin{aligned} E &= \frac{1}{2}mv_0^2 + U - mv_0 \cdot \Omega \times r \\ &= E_0 - mv_0 \cdot \Omega \times r \end{aligned} \tag{2.24}$$

that results in the transformation law from an inertial to a non inertial frame

$$E(K) = E_0(K_0) - M \cdot \Omega \tag{2.25}$$

So, to consider the energy as term of verification of the physical meaning of the system some steps must be done to adapt it to the frame of work, e.g adding the extra term referring to angular momentum when analysing the body frame. This is a useful derivation since many simulations have been done considering only the inputs of acceleration and rotation of the tank in the sloshing model, without considering the complete coupled equations. Otherwise the velocities and acceleration can be translated in inertial frame where energy conservation still holds.

2.3.2 Related Work

As historical component, liquid sloshing in spacecraft propellant tanks has been extensively studied since the early days of spaceflight. The initial work by Abramson [1] presented one of the first systematic analyses of the dynamic behavior of liquids in moving containers. Building upon this, Dodge and Garza [9] investigated low-gravity sloshing in spherical, ellipsoidal, and cylindrical tanks, providing empirical scaling laws still widely referenced.

Further contributions by Dodge and collaborators [8, 10] refined these models, leading to the development of *equivalent mechanical models*, which approximate the sloshing liquid as discrete masses with spring–damper connections. These analytical approaches remain essential for control-oriented modeling due to their computational efficiency [14, 15]. Instead, with the advancement of computational capabilities, high-fidelity numerical simulations have been adopted to study sloshing in low- and micro-gravity environments for the specific case treated but usually not generalizable. In particular, Yang and Peugeot [22] extracted sloshing parameters via CFD to enhance spacecraft attitude dynamics models, while Hahn et al. [12] analyzed nonlinear propellant sloshing and its effects on AOCS. Luppes et al. [19] also performed

numerical simulations of liquid motion under microgravity.

Recent approaches combine analytical models with CFD-derived coefficients for accuracy and real-time feasibility, as discussed by Bourdelle et al. [3] and Alazard et al. [2].

Beyond classical sloshing, low-gravity propellant management often involves capillary and multi-phase phenomena. Foundational work by De Gennes et al. [6] describes drops, bubbles, and wetting dynamics. Capillary and methods for propellant positioning have been explored by Collicott [4] and Hart et al. [13]. Bubble motion in spherical tanks was analyzed direct numerical simulation by Dalmon et al. [5], and oscillating drop techniques were revisited for low-gravity applications by Egry et al. [11]. Experimental campaigns have historically provided critical validation for sloshing models. Notable examples include the hydrazine tank slosh studies by Kana and Dodge [16] and the COLD-SAT cryogenic experiments [**NASA_Cold-sat**]. Drop tower and parabolic flight campaigns remain relevant for characterizing transitions from normal gravity to microgravity conditions [18].

Finally, recent research focuses on hybrid analytical–CFD models, multi-mode nonlinear sloshing, and the inclusion of thermo-capillary and cryogenic effects for long-duration missions. These trends aim to bridge the gap between the fidelity of CFD and the computational requirements of onboard control models.

Chapter 3

Methods

In order to describe the motion of fluid within a spacecraft tank, several aspects must be considered. Parameters such as the physical and chemical properties of the liquid, the geometry of the container, the type of external inputs applied to it, and the presence of devices inside the tank are just some of the factors influencing the dynamics. The fluid behavior follows the governing equations of fluid dynamics, obeying the conservation of mass, momentum, and energy, within the boundary condition of no penetration through the tank walls. These boundaries differ for each geometry, shaping the unique response of the system.

Numerical simulations and computational methods based on these equations achieve high-fidelity results. Post-processing these results allows for extraction values of key quantities then possibly integrated with further analysis. Examples of data extraction are the forces acting on the container walls, the excursion of the centre of mass (COM), and other parameters like the shape and size of the liquid-gas interface. The former group is essential for computing the spacecraft's overall dynamics and both the static and dynamic inertia of the subsystem and the whole structure. The latter, instead, is particularly important in describing the surface energy stored in the fluid during mission phases where capillary forces dominate over inertial and gravitational ones.

Moreover, modal analysis, often conducted using FEM, reveals the oscillation modes of the fluid. This information must be taken into account in the control algorithms implemented in the AOCS software to avoid resonance with main structure vibration modes or those of appendages (e.g., deployable booms or solar panels) and with the

control frequencies.

However, such numerical analyses are too computational expensive to be executed in an AOCS simulation, for which operational efficiency is an important aspect of evaluation. For this reason, data from experiments and simulations are gathered and processed offline to develop alternative, reduced-order models capable of delivering the necessary information to the onboard software. This knowledge is then used to perform active control via reaction wheels and thrusters, mitigating disturbances caused by fluid motion.

Based on these premises, the concept of the mechanical equivalent method is introduced. By applying the fluid dynamics equations to a general case, the liquid's behavior can be represented through a combination of well-chosen kinematic constraints and basic mechanical components.

This approach was originally developed by Abramson in [1] and has since been used in numerous studies, often validated through comparison with analytical solutions from fluid dynamics equations and numerical simulation results. The method offers a robust framework for modelling different sloshing behaviors under varying gravity levels and tank excitation profiles. The most relevant cases are presented in the following sections.

3.1 Justification of Mechanical Equivalence

When the precise fluid shape and detailed behavior are not a priority, the fluid motion can be represented using an equivalent mechanical model, which is easier to simulate and modify. This is precisely the case for sloshing behavior handled by AOCS software. The framework itself requires, as inputs from the slosh model, the forces and torques generated on the tank, the mass distribution of the fluid (to compute inertia), and the oscillation modes that might interact with other parts of the structure. All this information is fed to the control algorithm to dampen internal disturbances caused by fluid motion. The necessary knowledge is more related to the overall motion and mass displacement than to the precise surface configuration of the fluid, with some additional data on higher eigenmodes.

To accurately capture dynamic behaviors such as oscillations, forces, and dynamically changing inertia, the mechanical equivalent cannot rely solely on a rigid-body

representation of the fluid. This is demonstrated in [1] which considers a cylindrical tank with coordinates (r,θ, z) and its longitudinal axis directed along $+z$. The liquid reaches the height h , partially filling the container.

The velocity potential of the liquid Φ satisfies Laplace's equation:

$$\nabla^2\Phi = 0 \tag{3.1}$$

with boundary conditions at the tank walls:

$$\frac{\partial\Phi}{\partial n} = V_n \tag{3.2}$$

where V_n is the normal component of the tank velocity. Considering the potential, at the tank wall on the normal (n) direction it is constraint to have the value of V_n . At the free surface the potential follows

$$\ddot{\Phi} + g\frac{\partial\Phi}{\partial z} = 0 \tag{3.3}$$

The potential can be considered as the sum of two components $\Phi = \Phi_1 + \Phi_2$ where Φ_1 satisfies only Equations 3.1 and 3.1, while the Φ_2 represents the static behavior of a fully filled tank, subjected to the unsteady pressure from Φ_1. In this case, Φ_2 at the tank walls satisfies

$$\frac{\partial\Phi_2}{\partial n} = 0 \tag{3.4}$$

as homogeneous boundary condition, and for the free surface condition satisfies Equation3.1. This can be rewritten as

$$\ddot{\Phi}_2 + g\frac{\partial\Phi_2}{\partial z} = \dot{p}(t) = -\ddot{\Phi}_1 - g\frac{\partial\Phi_1}{\partial z} \tag{3.5}$$

Assuming that the tank is a rigid body, with x_0 being its time-varying displacement, the potential Φ_1 can be written as

$$\Phi_1(r,\theta,z,t) = \dot{x_0}\phi_1(r,\theta,z) \tag{3.6}$$

linking the fluid motion directly to tank motion, consistent with Equation 3.1.

Similarly, Φ_2 can be expressed in terms of the ordinary sloshing mode $\phi_{2,m}$ and the

coefficients $g_m(t)$:

$$\Phi_2(r,\theta,z,t) = \Sigma_{m=1}^{\infty} \dot{g}_m(t)\phi_{2,m}(r,\theta,z) \tag{3.7}$$

Substituting into Equation 3.1 and assuming $\frac{\partial \Phi_1}{\partial z} = 0$ at the free surface for the type of motion considered:

$$\ddot{g}_m + \omega_m^2 g_m = A_m \ddot{x}_0 \tag{3.8}$$

Here an oscillating dynamics becomes evident, indeed ω_m is the natural frequency of the m-th sloshing mode and A_m is a constant.

In order to compute the forces and torques on the tank walls, the pressure must be integrated over the relevant area. Pressure appears in Equation 3.1 bounded to the tank motion as

$$\ddot{x}_0\phi_1 + \Sigma_{m=1}^{\infty} \ddot{g}_m \phi_{2,m} \tag{3.9}$$

showing that two contributions are necessary: a rigid-body motion term and a more complex oscillatory term that a rigid-body analogy alone cannot represent. Therefore, only when all $\ddot{g}$ terms are directly proportional to $\ddot{x}_0$, the rigid body analogy suffices. In general, however, mechanical components such as spring-mass systems or pendulums must be included, with parameters chosen to satisfy the governing equations. This analysis is valid for rigid containers; elastic or deformable tanks would require additional terms and modified boundary conditions, which are beyond the scope of this thesis.

Several advantages can be gained from the use of mechanical equivalents. Visualization is greatly simplified, allowing AOCS engineers to work with equations and tune parameters without handling complex fluid dynamics directly. The choice of the parameters and the relevance of the elements included must be mentioned. Indeed, including all m eigenmodes, each with its oscillating mass m_m, would match the total fluid mass but may introduce unnecessary complexity relative to the marginal improvement in accuracy. Careful selection of the most relevant modes balances model fidelity with usability.

In general, the setup can be represented as in Figure 3.1.2, where the main parameters are represented. The mass of the liquid is divided into a static mass m_0, cantilevered to the spacecraft, and sloshing masses m_i, where i denotes the i-th sloshing mode. The sum of all these components, the pendulums and the static mass, yields the total fluid mass. However, in practical models used for real analyses, this balance is often not

strictly maintained due to the relative significance of higher sloshing modes compared to the first. In fact, the mass assigned to the first sloshing mode, m_1, is typically much larger than that associated with the second eigenmode, m_2. For control algorithms and oscillation analysis concerning their impact on the spacecraft structure, it is generally sufficient to consider only the first sloshing mode to achieve a realistic model. Only in cases where resonance occurs at higher modes, their contribution becomes non-negligible. In the context of spacecraft dynamics and typical maneuvers, this situation almost never arises.

Figure 3.1.1: Relevance of second slosh modes compare to the first slosh mode. Credits to Abramson, 1966.

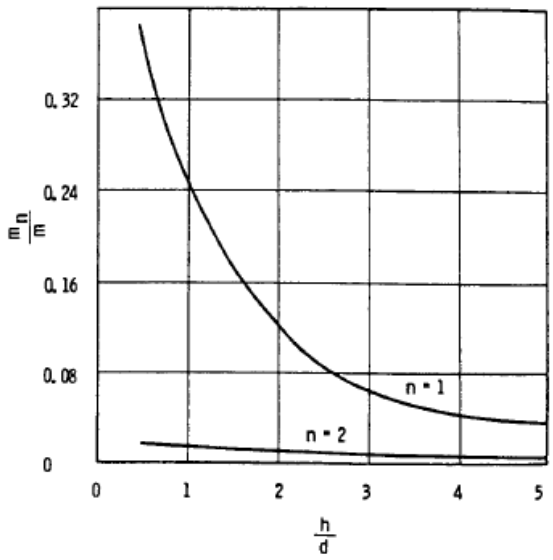

In Figure 3.1.1, the ratio of the sloshing mass assigned to the first mode to that assigned to the second mode is shown, expressed as a fraction of the total fluid mass. At low filling levels (or, in this case, low fluid height), the first sloshing mode accounts for an increasingly larger fraction of the total mass. This indicates that the fluid's behavior becomes predominantly non-static. In contrast, the second mode, which has at least an order of magnitude less mass than the first, remains almost constant with respect to the fill ratio, as does its contribution to the overall dynamics. Higher-order sloshing modes are associated with exponentially smaller masses, making their effect negligible for the purposes of an AOCS model.

In this thesis, in agreement with several works [**Dodge_1**, 1, 15], the sloshing model considers only the first mode. The mass assigned to this mode, m_1, varies with the fill ratio and the geometry of the tank, while the static mass is obtained by assigning to it

all the smaller masses of the higher modes:

$$m_0 = m_{\text{tot}} - m_1 \tag{3.10}$$

The pendulum model has the additional advantage of naturally incorporating the effect of gravity into its dynamics, so that it evolves intrinsically with the different phases of the mission. The parameters that need to be determined are the length of the pendulum rod L, the distance of the pendulum hinge from a reference point h_1 (usually the center of the tank), and the displacement of the static mass from the same reference point h_0. These parameters can be derived from experiments or simulations with a few adjustments. Following the determination of the pendulum parameters, the

Figure 3.1.2: General mechanical equivalent

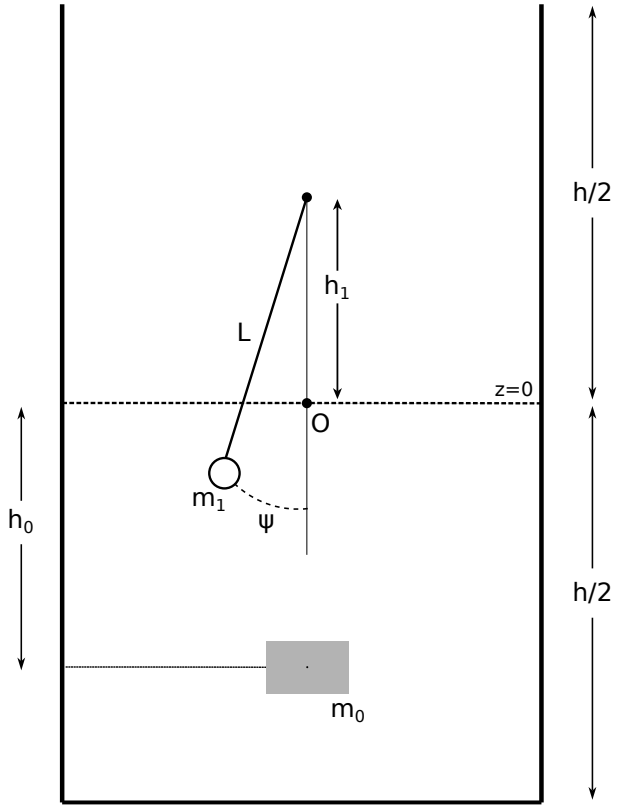

sloshing mass m_1 can be derived either from simulations or from experiments, where the response of the fluid to known force inputs on the tank is analyzed. The sloshing mass depends on both the quantity of fluid and the tank geometry. As shown in various studies [1], when the tank is nearly full, e.g., for fill ratios above 95%, the fluid can be satisfactorily represented by a static concentrated mass located horizontally at the geometric center of the tank. As the fluid volume decreases, the relative importance of the sloshing mass increases. However, in every set-up it is essential that the geometric

center of the liquid remains unchanged in the equivalent model with respect to its initial value. This is ensured by positioning the static mass below the center of mass according to:

$$h_0 m_0 = (h_1 - L_1) m_1 \tag{3.11}$$

The lenght of the pendulum L_1 and its natural frequency ω_n are related by

$$\omega_n = \sqrt{\frac{L_1}{g}} \tag{3.12}$$

Thus, knowing the resonance frequency of the sloshing fluid, it is possible to determine both L_1 and ω_n. Instead, the position of the hinge point h_1 can be derived experimentally by considering the maximum angular momentum and force on the tank when the motion is initiated and then rapidly stopped. This procedure is based on the definition of angular momentum with respect to the hinge point. An indicative evolution of h_1 with the fill ratio is shown in Figure3.1.3. where the dependence on the fill ratio is expressed using a more general tank geometry relation.

Figure 3.1.3: Hinge point evolution with fill ratio, expressed as ratio to the tank height. Credits to Abramson, 1966.

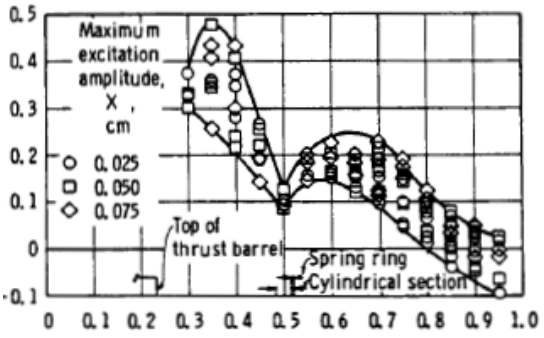

In general, deriving this parameter requires knowledge of the exact tank geometry, the type of fluid, and any potential internal devices. For the study conducted in this thesis, one of the objectives is to create a generalized model that can be applied to different projects where the AOCS subsystem may operate. For this reason, some analytical results are based on placeholders for the tank geometrical characteristics (height, width, and length for rectangular shapes; diameter for cylindrical tanks; semi-major and semi-minor axes for oblate shapes). These sets of parameters are based on the assumption that the tank is clean, without internal hardware or baffles, and that the liquid is inviscid.

Hereinafter, the graphics and plots representing the evolution of the parameters are presented. The numerical work of this thesis is based on parameters from a previous OHB project, which included a CFD analysis of the sloshing.

In the following sections, parameters for different shapes are presented.

3.1.1 Rectangular Tank

Figure 3.1.4: Rectangular tank parameters

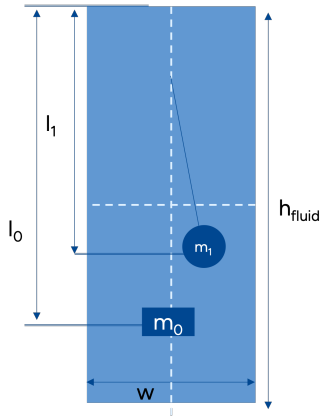

For rectangular tanks the parameters can be derived following the presented function taken from literature and that can be directly implemented in Simulink models, see Table3.1.1.

Table 3.1.1: Spring-Mass Analogy Model Parameters

Parameter	Expression
L_1	$\frac{w}{3.68}\coth(3.68\frac{h}{w})$
m_1	$m_T\left(\frac{w}{3.87h}\right)\tanh\frac{3.14h}{w}$
m_0	$m_T - m_1$
l_1	$\frac{w}{1.57}\tanh\frac{1.57h}{w}$
l_0	$\frac{h}{2}+\frac{m_1}{m_0}\left(\frac{h}{2}-l_1\right)$

Figure 3.1.5: Cylindrical tank parameters

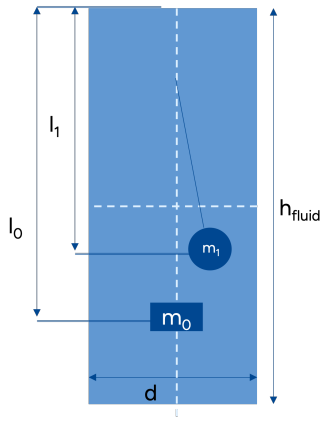

3.1.2 Cylindrical Tank

Also in this case, results are applied to the model from literature and can be inputted directly as in Table3.1.2

Table 3.1.2: Pendulum Analogy Model Parameters for Cylindrical Tank

Parameter	Expression
L_1	$\frac{d}{3.68}\coth(3.68\frac{h}{d})$
m_1	$m_T\left(\frac{d}{4.4h}\right)\tanh(3.68\frac{h}{d})$
m_0	$m_T - m_1$
l_1	$\frac{d}{7.36}csch(7.36\frac{h}{d})$
l_0	$\frac{m_T}{m_0}\left[\frac{h}{2} - \frac{d^2}{8h}\right] - (l_1 + L_1)\frac{m_1}{m_0}$

3.1.3 Spheroidal Tank

The results derived for spherical and spheroidal tanks include derivation of the fluid height and its relation with other parameters as it is not straight forward as in the precedent cases. Derivations are done for general spheroids, for which a sphere is a particular case.

For what regards spheroids, data are more sparse and functions describing parameters have not been computed generally. However, trends describing the evolution of each parameter are gathered from different literature sources (mainly [1] and [**Dodge_1**]). The relevant plots are digitalised and fitted to shape appropriate functions. Many

parameters had to be adapted to the analysis and handling of this model and the relative describing function are presented below 3.1.43.1.5. It is important to notice, that many studies have been conducted tracking fluid height instead of fill ratio (which is the ratio of volumes$fill_r = \frac{V(h_{fluid})}{V_{tank}}$). This aspect does not impact the use of results for rectangular and cylindrical tanks since the ratio of h_{fluid}/h_{tank} is the same as $V(h_{fluid})/V_{tank}$. However, when considering spheroids this relation does not hold anymore, and it is needed to define the analytical relation between fluid height and fill ratio. Indeed, many simulation environments uses fill ratio as input to the slosh model, therefore it is valuable to make this model accessible. The defining function for a general spheroid is:

$$\frac{x^2 + y^2}{a^2} + \frac{z^2}{c^2} = 1 \tag{3.13}$$

For a tank filled until the height h, the radius of the interface as h is:

$$r(h) = x^2 + y^2 = a\sqrt{1 - \frac{z^2}{c^2}} \tag{3.14}$$

and the area is consequently $A(h) = \pi a^2(1 - \frac{z^2}{c^2})$ The volume occupied when the fluid height is h comes from the integration of the area $A(h)$ over z for $z \in [-c; -c + h]$, and it results in:

$$V(h) = \big[z - \frac{c^3}{3c^2}\big]_{-c}^{-c+h}; \tag{3.15}$$

$$V(h) = \pi a^2\big[-c + h - \frac{h-c}{3c^3} + \frac{2c}{3}\big] \tag{3.16}$$

Considering now the ratio $V(h)/V_{tank}$ where $V_{tank} = \frac{4}{3}\pi a^2 c$, by definition called fill ratio:

$$fill_r = 3\eta^2 - 2\eta^3 \tag{3.17}$$

To derive this relation the substitution $\eta = h/2c$ has been implied. Considering the classic substitution for cubic function $\eta = (u + 1)/2$, this relation can be analytically solved to get the inverse relation. The final functions that from filling ratio gives fluid height for a spheroid is:

$$h(fill_r, h_{tank}) = \frac{h_{tank}}{2} \cdot \frac{1 + 2cos(\frac{1}{3}arccos(1 - 2 \cdot fill_r) + \frac{4\pi}{3})}{2} \tag{3.18}$$

This formula is of course valid for both oblate and prolate spheroids. Here are presented the function describing the relevant parameters for both this shapes. The

variable h here is made dimensionless as $h = H/0.5h_{tank}$ where H is actual fluid height in the spheroidal tank.

3.1.4 Spherical Tank

Figure 3.1.6: Spherical tank parameters

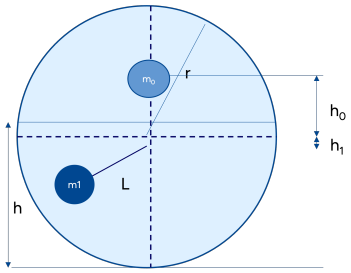

As particular case of what presented above, the spherical tank case can be described by parameters in the following table.

Table 3.1.3: Pendulum Analogy Model Parameters for Spherical Tank

Parameter	Expression
L_1	$R \cdot (-0.6145h^2 - 0.3323h + 0.9828)$
m_1	$\rho\pi h^2(R - h/3)\cdot$ $\cdot(0.01975 - 0.007715h + 8 \cdot 10^{-4}h^2 - 1.43 \cdot 10^{-5})$
m_0	$m_T - m_1$
$h_1 + h_{tank}/2$	$R \cdot (-6.618 * 10^5 h + 1.004)$
$h_0 + h_{tank}/2$	$R \cdot (8.43 \cdot 10^{-3} \cdot e^{-4.217h} + 1.065e^{-0.4247h})$
ω_1	$\sqrt{R/g}(1.319e^{0.1832h} + 0.0046e^{6.804h})$

3.1.5 Oblate Tank

Hereinafter are presented the results for an oblate spheroid.

Figure 3.1.7: Oblate tank parameters

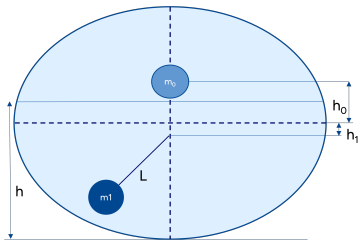

Table 3.1.4: Pendulum Analogy Model Parameters for Oblate tank

Parameter	Expression
ω_1	$0.6817e^{0.3863h}$
L_1	a_{eff}/ω_1^2
m_1	$m_T(-0.1009h^3 - 0.0234h^2 - 0.06943h + 09994)$
m_0	$m_T - m_1$
h_1	$\frac{h_{tank}}{2}(-1.845h + 3)$
h_{cg}	$\frac{3}{4}\frac{h_{tank}}{2}\left[\frac{(2-2h/h_{tank})^2}{3-2h/h_{tank}}\right]$
h_0	$h_{cg} + m_1/m_0(h_1 + h_{cg})$

3.1.6 Prolate Tank

Hereinafter are presented the result for a prolate spheroid.

Figure 3.1.8: Prolate tank parameters

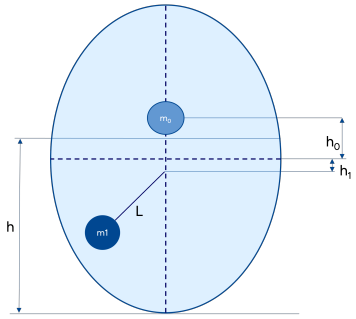

[**Rattayya, 1965**]

Finally, another useful aspect of substituting the fluid with a mechanical equivalent is the possibility of easily including elements to represent damping, as well as its evolution under different fluid conditions, depending on fluid volume, direction of excitation, or varying external environment. This is typically implemented, for example, with linear dashpots tuned as needed and added to the spring-mass or

Table 3.1.5: Pendulum Analogy Model Parameters for Prolate tank

Parameter	Expression
ω_1	$1.343e^{-0.09522h} + 0.004815e^{2.906h}$
L_1	a_{eff}/ω_1^2
m_1	$m_T(0.18h^2 - 0.818h + 0.952)$
m_0	$m_T - m_1$
h_1	$\frac{h_{tank}}{2} \cdot (-0.1272h^3 + 0.3624h^2 + 0.2852h - 0.6867)$
h_{cg}	$\frac{3}{4}\frac{h_{tank}}{2}\left[\frac{(2-2h/h_{tank})^2}{3-2h/h_{tank}}\right]$
h_0	$h_{cg} + m_1/m_0(h_1 + h_{cg})$

pendulum elements.

3.2 Damping

Tracking the total energy of the system can be a useful tool for assessing the reliability of a model. However, considering only the kinetic energy and gravitational potential energy of the masses in an inertial frame is not entirely accurate when the reference frame is initially attached to a fluid. The fluid nature implies complication on many aspect of the dynamics and among this is also its particle interaction in fluid-fluid and fluid-wall contact. With rare exceptions, fluids are viscous; they resist motion and dissipate part of the system's energy through viscous friction. This phenomenon applies equally also to the liquids contained in propellant tanks.

When sloshing motion is excited, the oscillation amplitude undergoes a gradual decay due to damping. For most common fluids, the damping ratio is relatively small, typically on the order of 10^{-2}.

Modeling damping in a real tank configuration is a highly complex problem, and no complete analytical solutions have been reported in the relevant literature. Nevertheless, several experimental studies have been conducted to determine damping values for specific cases. These studies indicate that the damping ratio depends on factors such as liquid height and tank geometry. In practice, it is often evaluated either experimentally, once the other system parameters are known, or via numerical simulation.

A common experimental approach involves applying a known impulse to the system. In this case, all parameters in the governing equations of motion are known except for the damping ratio, which can then be identified from the measured response.

The effect of computing the decreasing of the oscillations' amplitude is a way to determining damping ratio. Indeed, the decrease in amplitude can be represented with a logarithmic decrement as

$$\delta = ln \frac{\text{Max amplitude oscillation (cycle n)}}{\text{Max amplitude oscillation (cycle n+1)}} \tag{3.19}$$

In linear systems, since the displacement is proportional to the restoring force and its squared value is proportional to the total energy, the logarithmic decrement can also be expressed in terms of force or energy decrement. From the logarithmic decrement, the damping factor can be deducted from

$$\delta = 2\pi\gamma = 2\pi \frac{c}{c_c} \tag{3.20}$$

Where c is the actual damping coefficient of the system with dimensions [N·s/m] for linear damping, or [N·m·s/rad] for rotational damping. While c_n is the critical damping coefficient, which is the damping at which the system transitions from oscillatory to non-oscillatory behavior.

Although the damping ratio is small, its contribution to the dynamics of the chosen pendulum model remains significant and should be included. Given its generally acknowledged magnitude, a linear approximation is typically sufficient. Consequently, a damping term is introduced either as a linear dashpot or as a torsional component, depending on the specific form of the model. This approach is valid under the same assumptions for which fluid motion can be represented by the dynamics of a viscously damped single-degree-of-freedom system.

Experimental and numerical studies on two oblate tanks—available from different sources—show good agreement in their reported values of the damping ratio.

In the absence of simulation results tailored to the specific project under investigation, it is therefore reasonable to adopt, as an initial estimate, the values extracted from such studies when available. Therefore, in Table3.2.1 functions describing the evolution of fill ratio for high-g cases in different tanks is presented. The results are fitted functions combining experimental or analytical results from different sources with

agreeing results[8][15][1][10] and adapting them to the framework used in this project. Unfortunately, no data were covering the oblate tank case, that, however, can be approximated with a cylinder with same proportions.

Table 3.2.1: Damping ratio ζ for different shapes

Shapes	Expression
Cylindrical	$(5.538\left(\frac{h}{R}\right)^2 - 8.948\frac{h}{R} + 4.199)\left(\frac{\nu}{R^{1.5}\sqrt{a_{eff}}}^{0.5}\right)$
Rectangular	$\left(\frac{\nu}{w^{1.5}\sqrt{a_{eff}}}\right)^{0.5}$
Spherical	$(1.6\left(\frac{h}{R}\right)^2 - 0.92\frac{h}{R} + 0.45)\left(\frac{\nu}{R^{1.5}\sqrt{a_{eff}}}\right)$
Oblate	$(0.9516\left(\frac{h}{2b}\right)^5 - 0.9011\left(\frac{h}{2b}\right)^4 - 0.7354\left(\frac{h}{2b}\right)^3 +$
	$+1.221\left(\frac{h}{2b}\right)^2 - 0.5327\frac{h}{2b} + 0.08837)\left(\frac{\nu}{R^{1.5}\sqrt{a_{eff}}}^{0.5}\right)$

Where the damping is function of fluid height (the derivation of the relation fill ratio-fluid height is presented in the previous sections) and shape characteristic dimension: radius R for cylindrical and spherical tanks, w width for rectangular tanks, b semi-minor axis for oblate tanks.

The total damping of a fluid during excitation can also be increased through modifications to the tank geometry. Examples include the insertion of metallic baffles, elastic bladders, or other internal devices designed to dissipate energy and suppress sloshing amplitudes.

In the present work, damping is considered solely as a result of fluid viscosity. However, many experimental studies report data for configurations that also include internal hardware within the tank. To account for such effects, the plots and trends used in the damping analysis can be readily replaced with updated datasets reflecting the increased damping ratio. These updated values can then be incorporated into the analysis without requiring any changes to the underlying mechanical model.

The hardware employed for this purpose can vary in shape, thickness, and material, and in some cases may achieve near-complete suppression of oscillations. These devices can be either fixed or movable. A common example of fixed devices is baffles, which are rigidly attached to the tank walls and may differ in geometry and placement depth. Two frequently used configurations are annular and cruciform baffles. One of the most influential design parameters is baffle thickness, which tends to increase damping but also adds weight to the system. Examples of movable devices include

elastic diaphragms or expulsion bladders, in which the thickness of the material again plays a key role, though generally with less weight penalty compared to metallic components. Broadly speaking, the principle behind these devices is to either limit the motion of the free surface or reduce the available free volume in the tank, while preserving the overall geometry so that the global dynamics remain comparable. Sloshing in sectored tanks presents additional complexity and is beyond the scope of the present study.

Figure 3.2.1: Damping in oblate tank with cruciform baffles, Abramson,1966

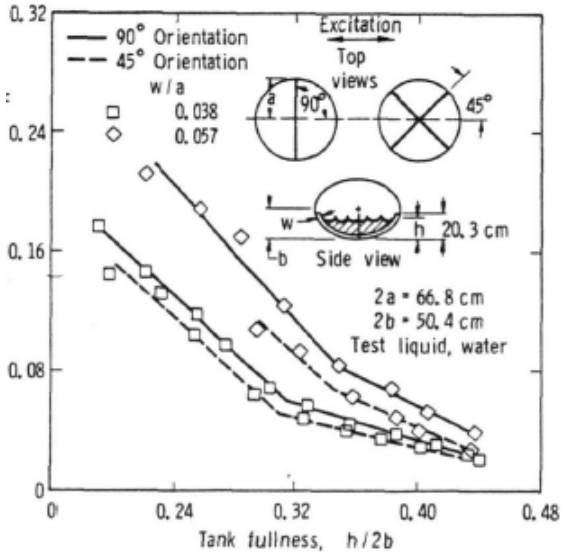

Figure 3.2.2: Damping in oblate tanks, Abramson,1966

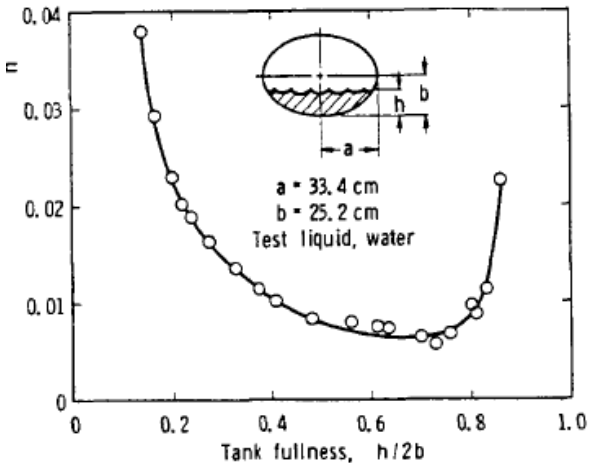

As an illustrative case in Figure3.2, a graph showing the effect of cruciform baffles in an oblate tank is presented to facilitate comparison and to evaluate the effectiveness of this type of device. While in Figure3.2.2, it can be seen the damping ratio for an oblate

tank without internal hardware. In this example, the damping ratio increases to nearly 0.1 for a half-filled tank—this is particularly significant since viscous damping ratios typically reach their minimum at this fill level. Under these conditions, the damping has increased from approximately three times its original value to nearly an order of magnitude higher.

3.3 Force Influence - Bond Number

The physical situation described in the preceding sections changes significantly when a tank filled with fluid experiences an acceleration several orders of magnitude lower than g_0, the average gravitational acceleration at Earth's surface. Under such conditions, the behavior of the fluid no longer follows the dynamics described above, as new forces become dominant. In particular, surface tension begins to outweigh both gravitational and inertial forces. This effect manifests primarily at the free surface, producing phenomena collectively referred to as capillarity.

The loss of dominance of body forces occurs when the net acceleration acting on the system—whether gravitational or inertial—decreases gradually or abruptly. This reduction does not require the acceleration to reach exactly zero; in fact, achieving a perfect null acceleration would necessitate a spacecraft being located far from any massive body exerting an appreciable gravitational influence, a scenario infeasible for the configurations considered here. In practice, weightlessness is achieved when the vector sum of gravitational acceleration and the body's own acceleration is zero. Under these conditions, the system is said to be in a state of free fall or apparent weightlessness.

Experiments aimed at studying fluid behavior in such environments are typically performed in drop towers or during parabolic flight campaigns. However, complete weightlessness is not always the most informative test condition. Experimental setups in microgravity—defined here as accelerations in the range of 10^{-3} to 10^{-6} m/s²—often yield more relevant insights for spacecraft applications, as they more closely replicate the low but nonzero acceleration levels encountered in orbit.

It is important to note that, aside from isolated studies, experimental data under these conditions remain limited. The complexity arises from the fact that fluid behavior depends simultaneously on multiple parameters, including tank geometry, fill ratio,

and relative acceleration. Consequently, it is not feasible to base a general analysis solely on experimental observations. Nevertheless, by relying on capillarity theory and the use of suitable dimensionless parameters, it is possible to predict fluid behavior for a given set of conditions. These predictions can then be incorporated into the modeling process, enabling the construction of a sufficiently representative model even in the absence of extensive experimental data.

3.4 Dimensionless Parameters

As discussed in the previous section, the relative influence of gravitational, inertial, and capillary forces can vary significantly during a typical spacecraft mission, depending on the operating mode and acceleration environment. Each of these forces may dominate at different phases, leading to markedly different fluid behaviors and interface shapes.

To identify the prevailing physical effects in a given condition, dimensionless parameters are often used. These parameters allow one to compare the relative magnitude of different forces, thereby indicating which effects can be neglected and which must be considered in the analysis of liquid propellant sloshing.

Two fundamental dimensionless numbers are:

- $We = \frac{\rho V^2 L}{\sigma}$, Weber number describes the relative importance of inertial and capillary forces.
- $Fr = \frac{V^2}{gL}$, Froud number describes the relative importance of inertial and gravity forces.

In the framework of a space mission, Weber number is mostly influenced by thrusting, so whenever the spacecraft it is not maneuvering, the environmental conditions (e.g. gravitational force) determine which dominance range the system falls into. It is important to notice how the scaling dominance of each force-type on the singular case, depend on the dimension of the tank and the fluid parameter greatly. For instance a smaller tank, given equal thrust, will have greater area for capillarity dominance than a bigger tank. Because of this, the most extensively used parameter, in the analysis of slosh, is the ratio of the two presented above: the Bond number.

$$Bo = \frac{We}{Fr} = \frac{\rho g L^2}{\sigma} \tag{3.21}$$

The Bond number represents the ratio between gravitational forces and surface tension forces. For spacecraft attitude dynamics and control, these two effects are of primary interest, as they typically alternate in dominance depending on the operational mode of the system.

Figure 3.4.1: Division of forces predominance based on dimensionless parameters.

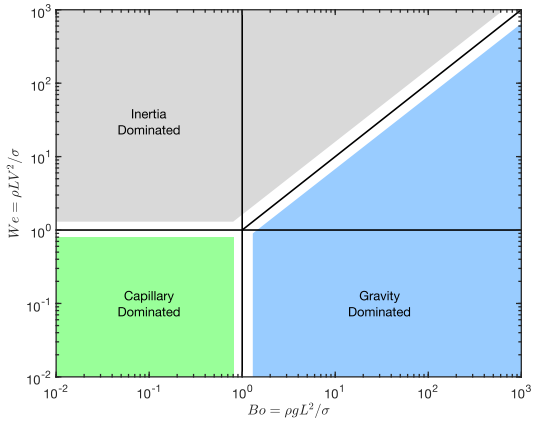

The graph reported in Figure 3.4.1 illustrates how the state of the fluid can be qualitatively classified according to the values of key dimensionless parameters. The Bond number, in particular, has been examined experimentally in tanks of various geometries and sizes. Its value provides insight into which forces dominate and, consequently, which physical effects are most relevant to the analysis. A commonly cited reference point is $Bo = 1$, at which the gravitational and capillary forces are of comparable magnitude. Empirical studies have shown that gravity-dominated behavior is generally observed for $Bo \geq 10$, while capillarity-dominated behavior is observed for $Bo \leq 0.1$. Examples of gravity-dominated regimes include large-amplitude oscillations with frequencies dependent on gravity level. In contrast, capillarity-dominated regimes may exhibit phenomena such as liquid climbing along the container walls and increased effective inertia.

In practice, the Bond number is primarily computed to assess how external conditions influence fluid motion in a given setup. This assists in selecting appropriate sensors and monitoring strategies for both simulations and physical experiments. However, thresholds reported in the literature are not typically used as strict criteria for modular dynamic modeling.

In the present work, the Bond number is employed as a key indicator to classify and analyze the different dynamic regimes that a spacecraft propellant tank may encounter during its mission profile. This parameter provides a physical basis for determining whether gravitational or capillary forces dominate the liquid behavior and, consequently, for selecting the most appropriate modeling approach for each case.

Based on this framework, three representative modes have been identified and modeled separately, reflecting the range of conditions that may arise in actual operational scenarios:

- High-acceleration mode: this regime corresponds to conditions in which $Bo \gg 1$, and gravitational forces dominate over surface tension effects. It typically occurs during thrusting or strong maneuvering phases. The sloshing dynamics are modeled using the classical mechanical pendulum analogy described in previous sections, which effectively captures large-amplitude oscillations driven primarily by gravity.

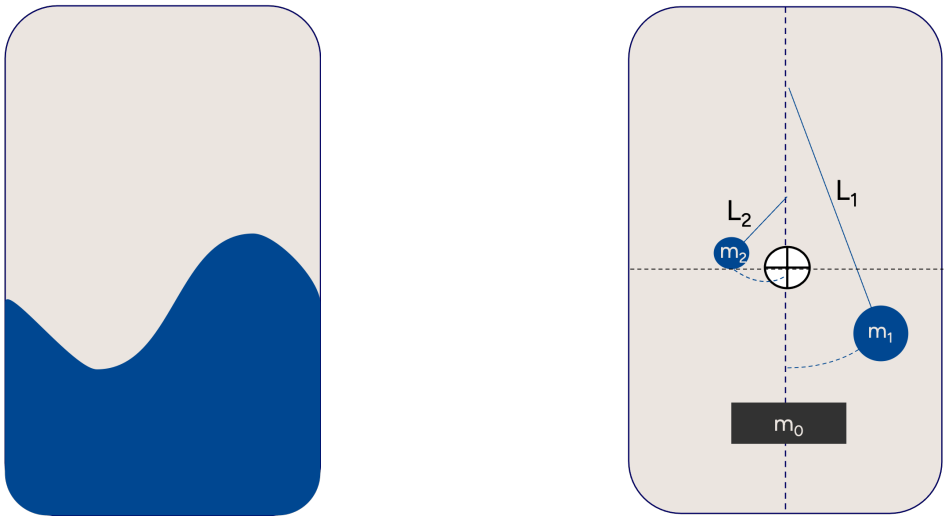

Figure 3.4.2: Fluid and mechanical representation of high-g behavior

- Low-acceleration mode: this regime corresponds to conditions in which $Bo \ll 1$, and surface tension is the primary driver of fluid configuration and motion. Such situations are common during long-duration coasting or orbital operations with very low residual accelerations. Here, a capillarity-based model has been developed to capture the characteristic redistribution of the liquid along tank walls, the alteration of the free-surface shape, and the resulting variations in the

fluid's inertia properties. This model focuses on how these changes affect the spacecraft's mass distribution and attitude dynamics.

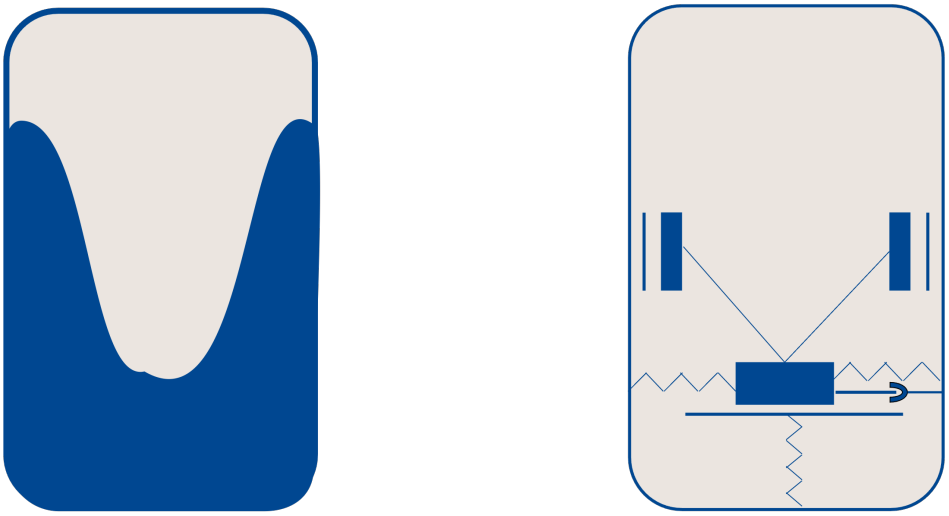

Figure 3.4.3: Fluid and mechanical representation of low-g behaviour

- Transitional or unstable configurations: these modes occur when Bo is near unity or when the system is perturbed from either a gravity- or capillarity-dominated state. Under certain disturbances, the liquid mass may break into distinct configurations that are however unstable.

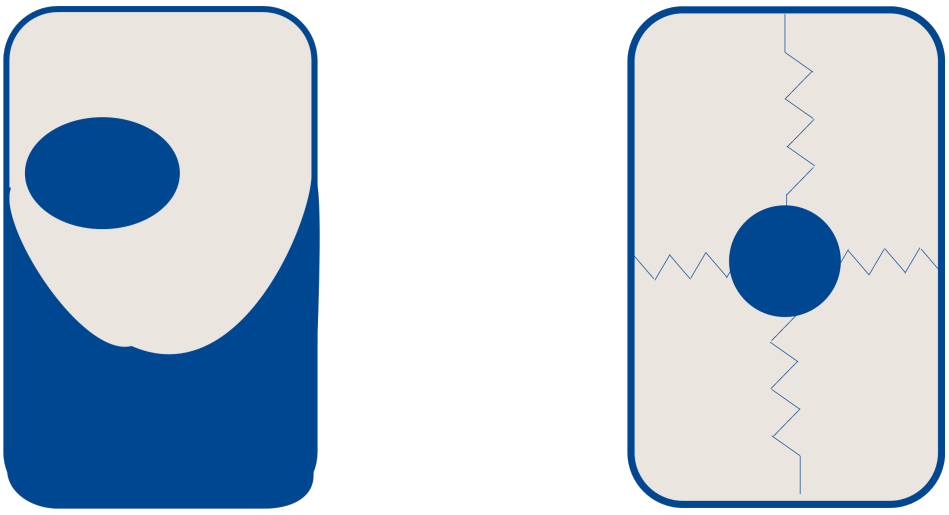

Figure 3.4.4: Fluid and mechanical representation of a drop transition configuration

Among transitional modes, particular attention is given to drop configurations, where a portion—or, in low fill conditions, nearly the entirety—of the liquid detaches from the main bulk and floats freely within the tank. This can lead to substantial and rapid shifts in the spacecraft's inertia and center of mass. In this state, the free-floating liquid does not directly respond to tank accelerations or store angular momentum

until recontact with the tank wall. Such configurations are generally transient, with the fluid eventually rejoining the main bulk or adhering to a wall, in accordance with the principle of minimum energy.

Instead, bubbles of air, where pockets of gas form within the fluid have not being modelled as independent mode. This is done under the assumption that their dynamics follows the same governing principles as the surrounding liquid, with the gas volume treated as part of the free ullage. In capillarity-dominated regimes, bubble geometry is represented implicitly by the curvature of the free surface. If a bubble migrates to another region of the tank, the model adapts to the new configuration without requiring additional equations.

By separating these regimes, the analysis can more accurately represent the physical behavior of the propellant in varying operational conditions. The following sections present the detailed modeling approach for each regime, along with their implications for spacecraft attitude and control.

An initial definition of the proposed framework can be seen in Figure3.4.5. The concept developed in this thesis is to provide a systematic method for predicting the fluid behavior inside the tank under different operating conditions, using only the information already available to the AOCS framework at any given time (e.g IMUs). By identifying the prevailing fluid behavior, the appropriate dynamic model can be selected for controller design or, alternatively, just to analyse the effects of maneuvers and external disturbances on the spacecraft. The switching mechanism is based on the Bond number, which determines the current mode of the fluid. Each mode is associated with a distinct set of dynamics, derived from experimental observations and supported by analytical fluid dynamics considerations. In theory, the combination of influencing parameters, such as geometry, acceleration level, fill ratio, and fluid properties, could lead to an infinite variety of configurations. In this work, the problem is reduced to a minimum of three representative dynamic modes:

Pendulum mode (Mode 1) and capillarity mode (Mode 2) represent two stable configurations of the fluid inside the tank. The fluid settles into one of these two modes depending on the level of acceleration, the tank geometry, and the surface tension σ of the fluid. While surface tension values remain relatively similar across the common propellants in use, the dependence on gravity level and geometry means that two tanks with identical shape and fill ratio but different sizes could be in opposite modes under

the same gravity level.

In transitional states - such as when an abrupt change in effective acceleration occurs, for example when switching from an idle state to a maneuvering (thrusting) state — a third configuration, referred to as drop mode (Mode 3), is considered. In this mode, a portion of the liquid may detach from the main mass and float freely within the tank. The drop shape follows the minimum-energy principle, forming a sphere to minimize surface area while floating, and then further reducing surface area upon attachment to a wall. From this transient state, the fluid eventually converges to either Mode 1 or Mode 2. Drop mode can also arise from perturbations in Mode 2, particularly under very low gravity levels, where small disturbances can cause portions of the liquid to detach and behave independently before rejoining the main mass.

Figure 3.4.5: Bond number-based switch condition

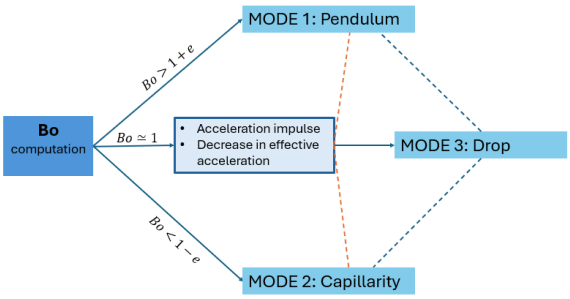

The equations of motion for the three modes are implemented in Simulink, with each mode encapsulated in its own subsystem containing the parameters required for its specific dynamics. The Bond number is computed in a higher-level block and serves as the switching condition to activate the appropriate mode.

This architecture allows the simulation to be directly integrated into AOCS analysis. The model receives as inputs:

- measured acceleration in the body frame;
- geometry of the tank;
- fluid properties;
- fill ratio.

From these inputs, it produces outputs reflecting the actual dynamics the fluid would experience under those exact conditions. This enables results grounded in

experimental and analytical knowledge without requiring real-time CFD or other computationally expensive fluid dynamics solvers, thus offering a computationally efficient yet comprehensive tool.

Furthermore, because the model accounts for the distinctive behaviors of each mode, it can provide more accurate estimates of static and dynamic inertia, as well as center-of-mass position—parameters that can vary significantly between modes and are difficult to capture with a single, unified model.

It is acknowledged that real fluid behavior is influenced by additional factors, such as tank wall cleanliness, fluid purity, and other subtle physical effects, making it unrealistic to define perfectly distinct modes in all cases. For this reason, the current implementation uses mutually exclusive switching conditions as an initial simplification. In later stages, the framework will incorporate smoother transitions, allowing multiple modes to be partially active in parallel. This progressive refinement is compatible with the Simulink implementation and will be detailed in the next chapter.

3.5 Capillarity Mode

After the pendulum configuration has been presented in the previous sections, with its analytical and experimental base, here Mode 2 is presented. In capillarity mode, corresponding to low Bond numbers, the general dynamics derived in the previous section still applies to some extent. The characteristic velocity remains $L\omega_n$. However, in conditions where surface tension forces dominate, the Froude number Fr is no longer the governing parameter; instead, the Weber number We becomes the key dimensionless parameter, as it captures the relative influence of inertial and capillary forces.

Before detailing the capillarity-dominated model, several important parameters and concepts must be introduced.

Surface tension arises at the interface between a liquid and a gas. The two phases maintain a pressure difference ΔP that must be balanced by surface tension for the interface to remain in equilibrium. According to the Laplace law, for a spherical bubble

of radius R, this balance is expressed as:

$$P_1 - P_0 = \frac{2\sigma}{R} = \frac{4\sigma}{D} \tag{3.22}$$

For a general curved interface with principal radii of curvature r_1 and r_2, the pressure difference is given by:

$$P_1 - P_0 = \sigma\left(\frac{1}{r_1} + \frac{1}{r_2}\right) \tag{3.23}$$

Surface tension values σ are usually specified for a liquid in contact with air, but they have been shown to apply with good accuracy when in contact with other gases. In this work, it is assumed that the values for air provide sufficiently precise results for the intended analysis.

Another critical parameter is the contact angle θ_c, defined as the angle between the tangent to the liquid-gas interface and the solid surface. This angle distinguishes wetting fluids from non-wetting fluids: wetting fluids have $\theta_c < 90°$, while non-wetting fluids have $\theta_c > 90°$, as illustrated by mercury on a solid surface. During motion, the contact angle may vary due to hysteresis, with different values for advancing (expanding onto an untouched surface) and receding (retracting on an already wetted surface) conditions. The contact angle is important because it affects the computation of surface tension forces, the associated energy, and consequently the shape of the liquid interface. For practical purposes in this model, it is considered sufficient to assume $\theta_C = 0°$, a common assumption that is valid for most propellants used.

3.5.1 Dynamics and Oscillation Properties

In capillarity-dominated conditions, the natural frequency of the fluid oscillations transitions from a gravity-based definition:

$$\omega_n^2(L/g) = A \tag{3.24}$$

to a capillarity-based definition:

$$\text{to be } \omega_n^2(\rho L^3/\sigma) = B \tag{3.25}$$

where A and B are parameters that depend on the fill ratio and tank geometry. It is important to note that the expression for natural frequency in low-gravity

conditions is independent of the actual value of g. This implies that the oscillation frequency does not vanish simply because gravity is not dominant. Indeed, some simplifications may treat the fluid in microgravity as nearly solid, due to the effect of capillarity resisting motion. However, this can be misleading: experimental observations indicate that when the effective acceleration abruptly decreases, the fluid oscillates slowly with frequencies ranging approximately from 0.001 Hz to 0.1 Hz, depending on tank geometry and fill ratio. These low-frequency oscillations can coincide with resonant frequencies of spacecraft structural components, potentially leading to physical damage or interference with control systems.

The sloshing behavior at high Bond numbers has similar characteristics to the low Bond number dynamics, but present an additional term to represent the new influence of capillarity. This can be a torsional spring connected to a pendulum hinge or linear dashpots. Indeed, at low-Bo conditions, the frequency is modified by surface tension effects:

$$\Omega = \frac{\omega}{\sqrt{(1+Bo)(\sigma R_0^3/\rho)}} \tag{3.26}$$

and results to be strongly bounded to fluid properties as density and surface tension and not to acceleration.

Figure 3.5.1: Dimensionless slosh frequency, first and second mode, with liquid depth $h > 2R_0$, Dodge, 1968

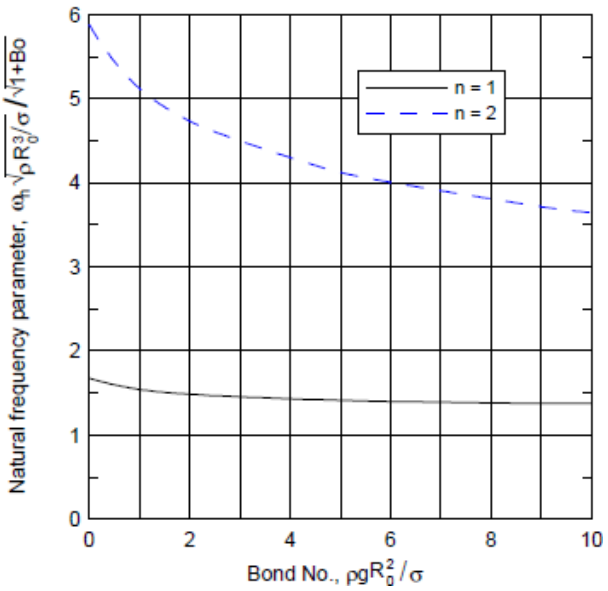

For $Bo \ll 1$, the natural frequency becomes practically independent of the Bond number.

The governing equations for low-gravity fluid sloshing follow a similar pattern as for high-g sloshing, but now include constraints to preserve the equilibrium contact angle, which is no longer negligible. The complete derivation is beyond the scope of this thesis, but can be found in [7]. These equations can be solved analytically using dimensionless parameters representing tank geometry, oscillation frequency, and wave amplitude. Solutions are obtained by computing eigenvalues and eigenvectors that satisfy the governing equation for a low-g sloshing tank.

In general, the solution has the same formal structure as the pendulum equivalent:

$$\omega_n^2 = \Omega_n^2 \left[\frac{g}{R_0} + \frac{\sigma}{\rho R_0^3} \right] \tag{3.27}$$

However, this result highlights the additional surface tension term, which acts as a stiffening element in low-g conditions. Mechanically, this is what an additional torsional spring at the pendulum hinge or a linear dashpot would represent. Compared to the torsional spring in a pendulum setup, linear dashpots allow the design of new configuration in Mode 2 that aims to represent the behavior more accurately for AOCS purposes. Therefore a different mechanical equivalent has been modeled to be included in the dynamics of the spacecraft and represent not only the right sloshing modes but also other parameters like inertia and mass distribution.

Some parameters need to be discussed regardless the model chosen. In particular,

- **Oscillating mass:** Analytical results for cylindrical tanks show that sloshing mass decreases as Bo decreases, with approximately 10% lower mass at $Bo = 10$ compared to $Bo = \infty$ [1, 7]. The same trend of sloshing mass can be considered for the case of rectangular tanks, because the underlying analytics refers to the same evolution. In this way, a coherent input data is ensured for the model. Moreover, prediction with similar analytical base are available for spheroidal tanks and the result can be sufficiently representative for spheroidals as well. Figures 3.5.2 and 3.5.3 illustrate the sloshing mass evolution as a function of fill ratio and Bond number.

  From the evolution shown, it can be seen that even though at $Bo = 10$ the value of sloshing mass decreases slightly from values of high sloshing, the evolution is smooth and continuous to values in the uncertain range of 1-10 Bo and and

Figure 3.5.2: Evolution of sloshing mass to total mass ratio with Bo and fill ratio as varying parameters

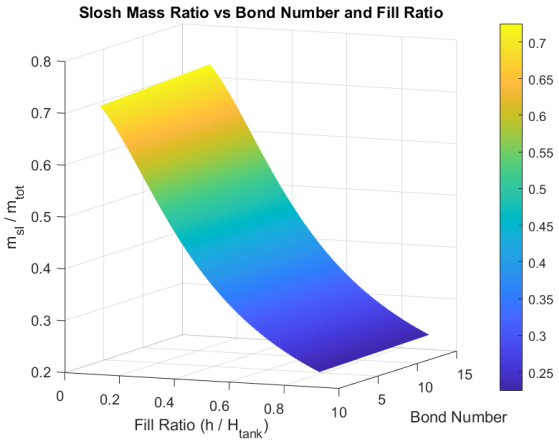

Figure 3.5.3: Evolution of sloshing mass to total mass ratio with Bo and fill ratio as varying parameters

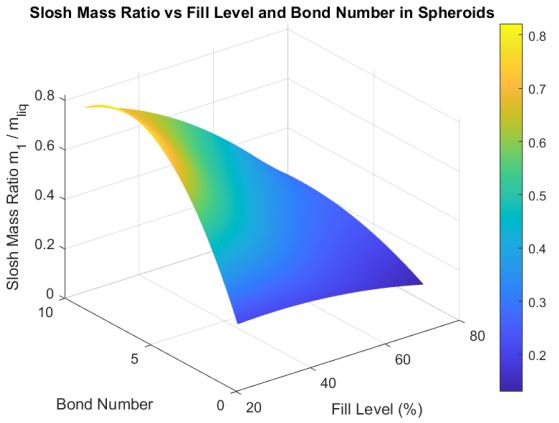

below, in the region of capillarity dominance. This is important and valuable for a switching condition that makes more than one mode being dynamically solved at the time.

- **Low-g slosh modes:** Oscillation frequencies decrease significantly compared to high-g sloshing. From experimental and simulation results, it appears that the frequency has markedly different values for spheroids and cylindrical/rectangular shapes. Spheroidal tanks tend to have slightly higher frequencies for equivalent fill ratios than cylindrical or rectangular tanks. In the capillarity-dominated model, only the first mode is considered due to limited experimental data. As general pattern ω_n decrease as fill ratio decreases. Although the dependence on the Bond number is embedded in the computation of ω as surface tension substitutes the dominance of the restoring

force in gravity. As can be deduced from Equation 3.22, a larger tank has a lower frequency, and for higher surface tension, the frequency will increase.

- **Damping:** sources of data for damping in low-g conditions cover only partially the different geometries, fill ratio, and Bond number. Some experiments conducted on cylindrical tanks show that for low Bo, damping ζ scales with the inverse of Reynolds number, Re, and to the fluid viscosity ν[7]:

$$\zeta = 4.47\sqrt{\frac{\nu}{\omega_1 R_0^2}} \tag{3.28}$$

  This observation provides useful insight, although it is not yet proven to be generalizable to all tank shapes. Nevertheless, it serves as a valuable reference for comparing magnitudes and trends. To characterize Mode 2 damping, data from experiments on various tank geometries have been analyzed and fitted against observations from different low-gravity setups. Additional trends for damping can also be inferred from settling time measurements and force response curves.

  In general, damping tends to increase under low-gravity conditions, partly due to larger wetted areas and enhanced viscous effects. However, these factors alone do not fully explain the observed increase. Despite the higher damping values, the system remains underdamped, with oscillations decaying gradually over time.

Here after are presented the numerical findings from literature results combination. The first low-g slosh mode is presented for spherical and oblate tanks as function of both fill ratio $fill_r$ and Bond number Bo. The range that is relevant to observe for this model is 1-10 Bo and $Bo < 1$. It is in general more common to find data for the former. However, for a first version of the model, the values found are good representations of the physical behavior, shaping satisfying results for the shapes considered in the model. Particularly, ω_1 is presented for cylindrical, spherical and oblate shapes, and for rectangular tanks the accuracy is good using a cylindrical equivalent sized model. Slosh mass for the spherical tanks is shaped on experimental trends and can be used for spheroids as well, since experiments conducted on oblate spheroids agree well with the spherical tanks findings. The cylindrical and rectangular cases are based on the assumption that the trend of slosh mass as function of fill ratio is the same but scaled in high-g and low-g, with the magnitude decreasing with Bond number. This assumption is verified in some experimental results, noticing the slosh mass at $Bo = 10$ is 10%

lower that at high Bo. [7][8]This linear trend is taken for low-g modeling, to shape a slowly decreasing function which maintains the same shape as in high-g. Damping for cylinders is represented by two functions for the range respectively of $Bo > 5$ and $Bo < 1$, noticing the logarithmic trend for damping as function of a decreasing Bond number, the two functions are interpolated to have continuity also in the mid-range. [7] Damping for sphere and spheroids is derived from experimental results and shaped as function of fill ratio.

Low-g slosh mode ω_1:

- Cylindrical: $0.2001e^{-1.9f_r} + 1.484e^{0.01255f_r}$ $\omega_1 = 1.61[\frac{\sigma}{\rho R}(1 + 0.798Bo)]^{0.5}$ and when h<3R $\omega_1 = 1.61[\frac{\sigma}{\rho R}(1 + 0.798Bo)]^{0.5} \cdot (tanh(1.841h/R))$

- Spherical:$a_0(Bo) + a_1(Bo) \cdot f_r + a_2(Bo)f_r^2$ where

$$a_0 = -0.0053x^2 + 0.0678x + 0.1148$$
$$a_1 = 8.7 \cdot 10^{-4}x^2 + 0.0175x + 0.0607$$
$$a_2 = -0.0164x^2 + 0.2309x + 0.3050$$

- Oblate:$a_0(Bo) + a_1(Bo) \cdot f_r + a_2(Bo)f_r^2$ where

$$a_0 = 0.0065x^2 - 0.119x + 0.2009$$
$$a_1 = -0.0156x^2 + 0.2093x + 0.3546$$
$$a_2 = -0.0069x^2 + 0.1331x - 0.1306$$

Low-g sloshing mass m_1:

- Cylindrical:$\frac{D}{4.4H}tanh\left(\frac{3.68H}{D}\right)\left(0.9 + 0.1\frac{Bo-10}{90}\right)$ and when implemented, the scaling factor can be clipped in $[0.5, 1]$.

- Spherical:$0.0781 + 0.0025f_r + 0.1434Bo - 0.0008f_r \cdot Bo - 0.0059Bo^2$

- Oblate: $0.0781 + 0.0025f_r + 0.1434Bo - 0.0008f_r \cdot Bo - 0.0059Bo^2$

Low-g damping ratio ζ:

- Cylindrical*:

$$\text{0<Bo<1:}\zeta_{0_1} = 4.47\sqrt{\frac{\nu}{\omega_1 R^2}}$$

$$\text{1<Bo<5:}(1+w)\cdot\zeta_{0-1} + w\zeta_5$$

$$\text{Bo>5:}\zeta_5 = 0.097\big(1+\frac{8.20}{Bo^{0.6}}\big)\sqrt{\frac{\nu}{\omega_1 R^2}}$$

$$\text{where } w = \frac{(log_{10}(Bo) - log_{10}(B))}{(log_{10}(5) - log_{10}(1))} = \frac{log_{10}(Bo)}{0.6990}$$

- Spherical:$a_2 \cdot f_r^2 + a_1 \cdot f_r + a_0$ where

$$a_2 = -0.077(log_{10}Bo) + 0.977$$
$$a_1 = 0.0556(log_{10}Bo) - 0.1353$$
$$a_0 = -0.0312(log_{10}Bo) + 0.0717$$

- Oblate:$a_2 \cdot f_r^2 + a_1 \cdot f_r + a_0$ where

$$a_2 = -0.077(log_{10}Bo) + 0.977$$
$$a_1 = 0.0556(log_{10}Bo) - 0.1353$$
$$a_0 = -0.0312(log_{10}Bo) + 0.0717$$

* The trend of Bo is fitted as piece-wise function to comply with literature results.

3.5.2 Shape and Geometrical Configuration

A key characteristic of the capillarity-dominated regime is the shape that the fluid adopts. In this regime, the force that normally keeps the fluid surface horizontal becomes negligible, allowing capillary effects to dominate. As a result, the liquid tends to cling to the walls and rise along the tank borders relative to the central region.

The configuration of the fluid surface is governed by thermodynamic principles and energy minimization. While a detailed derivation is available in several sources [8], an intuitive explanation is presented here to illustrate how the fluid surface evolves.

Consider a cylindrical section connected at its diameter to a cone on each side. If the two conical borders are pulled apart, work is applied to the section. The work, ΔW, is equal to the surface tension multiplied by the change in wetted area after the fluid

configuration is perturbed. When the contact angle θ_c is constant, the wetted area can be expressed as:

$$A_{\text{capillarity}} = A_{\text{interface}} - \cos\theta_c A_{\text{wet}} \tag{3.29}$$

Considering the energy balance on the system, assumed isothermal:

$$\Delta U = \Delta Q + \Delta W \tag{3.30}$$

where U is the internal energy and ΔQ is the heat transfer. For an isothermal and reversible process, we also have:

$$\Delta Q = T\Delta S \tag{3.31}$$

where S is the entropy and T is absolute temperature. If the tank reaches the equilibrium configuration only due to external conditions, e.g. microgravity, no work is performed. Therefore the expression in Equation3.5.2 becomes $\Delta U = \Delta Q$ Regarding the contribution of entropy change, for the second law of thermodynamics it holds $\Delta Q \leq T\Delta S$ which, combined with the previous expressions, yields:

$$T\Delta S = \Delta U - \sigma\Delta A_{\text{capillarity}} \quad \Rightarrow \quad 0 \geq -\sigma\Delta A_{\text{capillarity}} \tag{3.32}$$

and because σ can only have positive values, it follows that $\Delta A_{capillarity} \leq 0$. This shows that when capillarity dominates, the fluid adopts a configuration that minimizes the capillary area, i.e., the interface surface. For a given liquid volume and $\theta_c = 0$, a hemispherical configuration achieves the lowest capillary area compared to a flat surface.

In a hemispherical configuration, the interface radius of curvature matches half the tank width or radius. The fluid height at the lowest point is approximately one-third lower than the level of a flat interface. Basic geometric considerations, such as the center of mass of triangles, explain this height distribution for an incompressible fluid. While the hemispherical interface has a slightly larger surface area than the flat alternative, the increase in wetted area dominates, resulting in a more negative $\Delta A_{\text{capillarity}}$ according to Equation 3.29.

This new configuration does not directly alter the oscillatory behavior of the fluid, but for mid-filled tanks it significantly changes the mass distribution. It is therefore important to track the resulting changes in inertia in the AOCS database. Typically,

experiments and simulations focus only on impact forces on tank walls and do not account for the geometric variation of the interface. However, scientific studies of fluid behavior in microgravity provide photographic and analytical data that can inform the mechanical equivalent model, particularly for Mode 2 in capillarity-dominated conditions.

The same principle applies to free-floating drops and Mode 3. Fluid drops tend to merge to reduce their interface area, ultimately forming a single sphere. For any contact angle θ_c, a free-floating drop has a larger capillary area than one attached to the tank walls. Therefore, the stable configuration of a drop corresponds to attachment to the walls, consistent with the geometries seen in Modes 1 and 2.

3.5.3 Mode 2 Physical Model Description

Information required to develop a physical model that represents all relevant features and data for analysis within an AOCS simulator is generally not easy to obtain. Most experiments and simulations have different objectives, so data are often fragmented. However, by collecting results from multiple sources and cross-checking them, some trends have been identified and used to construct a new, representative model.

This mechanical equivalent is intended to capture the most significant aspects of fluid motion in capillarity-dominated tanks. These include the oscillation frequency, the forces generated by fluid movement, and the mass distribution, which determines the system's inertia. The reference model is illustrated in Figure 3.5.4.

The sloshing mass is divided into three main blocks: the largest portion is assigned to the central mass, m_3, while two equal lateral masses, m_1 and m_2, complete the total sloshing mass.

The central mass rests on a raised platform to match the total center of gravity of the fluid not involved in surface curvature. The platform can move vertically, compressing a spring k_{3_z}, mimicking the extension of the meniscus under longitudinal accelerations or rotations. The central mass can also move horizontally along a skid, constraining the positions of m_1 and m_2, which are linked to m_3 via a rigid rod. The lateral masses have fixed horizontal positions, while their vertical motion is guided along slides following the tank walls.

This design replicates the rise of fluid along the tank walls, producing a hemispherical

Figure 3.5.4: Mode 2 physical model

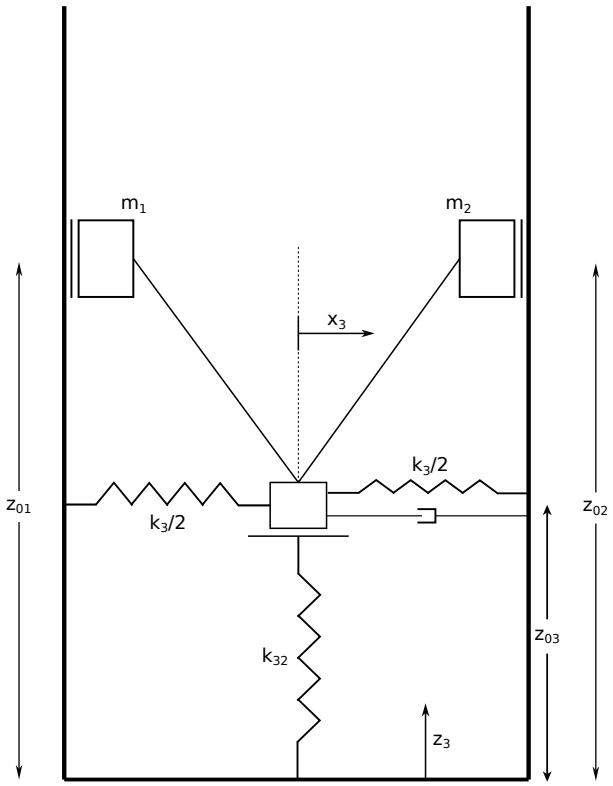

surface in cylindrical and rectangular tanks, or a hemi-elliptic surface in spheroidal tanks. For half-full or less-full tanks, the portion of fluid rising due to capillarity can be significant, sometimes exceeding 40% of the remaining volume.

These hemispheres or hemi-ellipses can be approximated in cross-section as triangles relative to the horizontal height of the lowest point of the interface. Following the geometric center of these triangles, the positions of m_1 and m_2 are determined both horizontally—at one-third of the triangle base from the wall—and vertically, at one-third above the peak of curvature. The central mass, m_3, is placed midway to the lowest point of the curvature to represent the remaining distribution.

The central mass has two degrees of freedom and interacts with the lateral springs k_3 and a linear dashpot as a damping element. These parameters drive the oscillatory motion of the central mass while the lateral masses compensate for volume conservation, maintaining the meniscus shape. Under a perturbation, for example, if the fluid is pushed toward one side, the fluid in low-gravity conditions will slowly cling to that wall, while the opposite side follows the motion more gradually, decreasing in height but preserving the curved interface pattern. Experimental observations, such as those shown in Figure 3.5.5, can aid in visualizing this behavior.

Figure 3.5.5: Experimental observation in low gravity. The surface maintains a curved interface on both walls edges even when the horizontal position of the center of mass is moved

Values for the spring constants and damping coefficients are derived from simulations, considering oscillation frequency, decay time, and damping ratio.

The relative quantity of fluid contributing to lateral distribution depends on the fill ratio, so model parameters are updated accordingly. In tanks with variable cross-section, such as oblate shapes, the surface dimensions change with fill ratio, requiring updates to both the horizontal and vertical equilibrium positions of the masses.

At high fill ratios, the gas bubble above the fluid is well represented by the curvature of the interface and the remaining tank volume, particularly in curved tanks. The fluid's position in the tank is determined by the most recent acceleration or pseudo-acceleration experienced. For an impulsive step down to microgravity, the fluid initially responds as if accelerated in the opposite direction. The system then reconfigures in Mode 2 according to the effective acceleration, with the final position from Mode 1 used as the initial condition. In realistic scenarios, the tank is rarely at rest before entering microgravity, so this initial configuration is typically known.

For simulations starting directly in microgravity, the model can begin in a chosen configuration relative to the body frame. If in-tank sensor data are available, these measurements can be incorporated as initial conditions for the fluid configuration.

3.6 Drop Mode

The third configuration considered in this work is the drop mode. In this mode, part of the fluid under certain perturbations detaches from the main mass and, through coalescence of smaller drops, forms a single drop or blob. This behavior occurs when surface tension acts on the fluid and competes with other forces. As discussed in

the surface energy considerations, the configuration of a floating drop is inherently unstable. It represents a transient fluid distribution that will eventually rejoin the main fluid mass or move toward the tank walls if no other fluid is present.

Understanding this dynamics is useful for analyzing transient moments between maneuvers or during transitions in mission phases. In such situations, relying only on stable configurations may fail to capture the complexity of the actual fluid behavior.

Drop mode is typically activated during transitions between accelerated (high-g) conditions and capillarity-dominated (low-g) conditions, and vice versa. It is also relevant at low fill ratios: when the fluid is in Mode 2 and experiences an impulsive acceleration insufficient to trigger a complete transition to Mode 1, experiments show that the fluid can fully detach from the wall and move as a drop until it reaches the wall again.

Early studies by Rayleigh demonstrated that oscillations of a drop under perturbation distort its surface from equilibrium. The restoring forces in this case arise solely from surface tension. When viscosity is included, small oscillations experience damping, but because the drop does not impact the wall, effective damping is much lower than in capillarity-dominated or high-g sloshing.

For a drop that does not come intooes not come into cont, thect with the tank, the rotation of the tank does not directly influence its motion; therefore, the drop does not store angular momentum that could affect the spacecraft. The drop itself may rotate, but this rotational motion has minimal relevance to the overall analysis and is not considered. Instead, it is sufficient to model the translational movement of the drop, which is sustained by springs representing the dynamical properties of this configuration.

More in detail, The oscillatory behavior of drops has been studied for centuries, starting with Rayleigh and more recently using optical observations of various liquids. The eigen-frequency of a non-viscous, force-free drop, which assumes a spherical shape in equilibrium, is given by:

$$\omega_l^2 = l(l-1)(l+2)\frac{4\pi}{2}\frac{\sigma}{M} \tag{3.33}$$

Here, ω_l is the eigen-frequency, σ is the surface tension, M is the drop mass, and l is an integer representing the mode of oscillation. The lowest frequency, known as the

Rayleigh frequency, corresponds to $l = 2$:

$$\omega^2 = 8\frac{4\pi}{3}\frac{\sigma}{M} \tag{3.34}$$

This expression can also be represented in terms of density and radius, as the equilibrium configuration inherently links these parameters. In practical terms, it is often convenient to consider the percentage of the total fluid mass assigned to drop mode and derive the corresponding volume. However, experimental data on drop mass are scarce and vary with fill ratio. Despite these uncertainties, the drop-mode setup remains valuable in the overall model and is easily tunable.

More recent studies [11] have incorporated the viscous contribution to the theory, defining a damping constant as:

$$\Gamma = \frac{20\pi}{3}\frac{R}{M}\nu \tag{3.35}$$

where ν is the kinematic viscosity. This damping is small relatively to the oscillation frequency, which can therefore be considered effectively unchanged. These results are valid for free-force environments such as microgravity and are assumed to apply during transitional conditions, effectively slowing down the drop motion without altering its primary oscillatory behavior.

3.6.1 Mode 3 Physical Model Description

The portion of fluid that detaches from the main mass due to residual velocity, inertia, or interface deformation depends on the tank's condition. The predominant parameter affecting the amount of mass in the drop is the fill ratio. Consequently, the size of the drop increases as the fluid height decreases. Experimental observations indicate that for fill ratios below approximately 0.20 and very low Bond numbers, stable equilibrium configurations can consist of entirely free-floating blobs or drops partially attached to the walls [**NASA_Cold-sat**][21]

In general, for fill ratios around $0.1 - 0.15$ or lower, during transitions or disturbances in microgravity, nearly 90–100% of the fluid can be considered to collect into a single drop. This behavior contrasts sharply with high fill ratio conditions, where any formed drops are small and quickly merge back into the main fluid mass, becoming almost negligible. An empirical formula for assigning mass to the drop, based on experimental

observations, is:

$$\frac{m_{drop}}{m_{tot}} = 0.7(1 - C)^{1/2} \tag{3.36}$$

The remaining fluid mass is treated as a solid ”brick” centered at the remaining liquid center of mass, which does not participate in the drop dynamics.

The drop is modeled as a spherical mass. Its relative volume and surface area are computed using standard geometric relationships. The case where the sphere diameter exceeds the tank dimensions is generally ignored, as high fill ratios produce small drops constrained within a small volume, while at mid and low fill levels the drop remains free to move. Nevertheless, for numerical stability and physical consistency, it is recommended to impose a maximum drop radius based on the fill ratio and tank geometry. If computations yield a radius exceeding this limit, the maximum allowable radius is enforced.

The drop is modeled as a rigid sphere floating freely within the tank. Physically, the drop is deformable, maintaining constant volume. Surface tension acts like an elastic membrane, resisting surface area increases. When the drop is perturbed, its deformation stretches the sphere, which then responds by restoring its shape. This behavior is modeled using springs that push and pull the sphere back toward equilibrium, as illustrated in Figure 3.6.1.

The drop is modelled as a rigid sphere floating in the middle of the tank, with no forces applied to it and so in equilibrium. The drop it self wound not be a rigid body, but a deformable mebrane that keeps a constant volume. The deformation, coming from surface tension, can be considered having elastic properties. This is because surface tension acts agaist any surface increasing action. In practice this results in a higher inertia while part of the mass is brought to follow the direction of the perturbation. Since the volume needs to stay constant, the deformation stretches the sphere, which it self responds to the impulse pulling back in shape the fluid. This mechanism is modelled with springs that pull and push back the solid sphere as shown in Figure3.6.1.

The potential energy of the drop is proportional to its surface area:

$$V = \sigma \cdot A \tag{3.37}$$

where σ is the surface tension. The condition of minimum potential corresponds to the

Figure 3.6.1: Mode 3 physical model

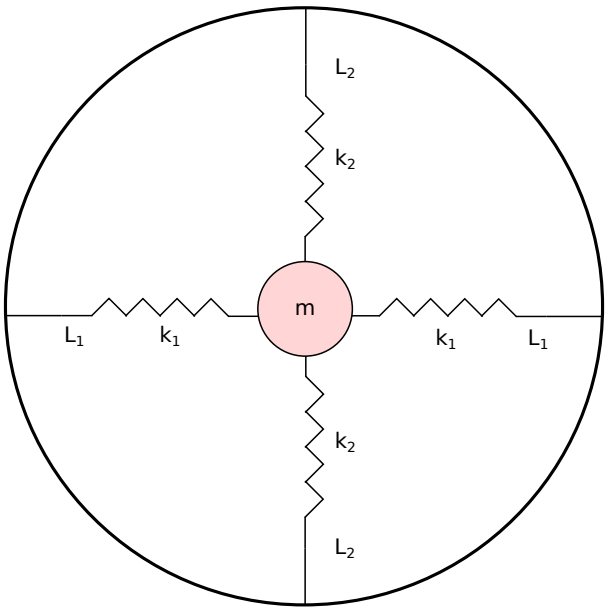

condition of minimum area - the sphere. This means that for small deformations

$$V_{surface} = \sigma \cdot (A_0 + \delta) \approx \sigma A_0 + \frac{1}{2} A_0 + \frac{1}{2} k_{eff} (\text{deformation}^2) \tag{3.38}$$

The reaction of the fluid to the new shape can be represented with an equivalent spring constant distributed along the surface, multiplied by the deformation from the spherical surface. While an ideal model would use an infinite number of springs radially distributed, a simplified approach divides the equivalent spring constant k_{eff} $n = 4$–6 springs- for either a planar or three-dimensional representation. This allows the solid sphere to distribute the response to the deformation on different directions within the axis of the coordinate system.

The spring constants are derived from the oscillation frequency due to surface tension (3.6) and the relation $k = \omega^2 m$: $k = \omega^2 m$:

$$k_i = \frac{32\pi\sigma}{3 \cdot n}, \quad i = 1, \ldots, n \tag{3.39}$$

where, in general the value of n can be increased with no limits if the dynamics of the system is updated. The springs are attached to the tank walls, bottom and top. Firstly it has been considered to make the spring statically attached to the mid-point of the tank wall, bottom or top, to restore from all directions the drop at the center. However, also an alternative approach has been presented since the former could not result physically

accurate. Particularly, there is lack of clear evidence that the deformation of the sphere is opposed by the fluid also for displacement of mass from the initial point and not only for the shape. Therefore, the elastic potential has been kept only to restore the sphere shape but not to push back to the center the sphere. This is translated in physical properties having all springs on skids. In this way springs would follow the movement of the sphere and then restore it on each axis. The restoring force in this way acts in the direction of the deformation only, slowing down the motion as expected.With sliding springs there is no representation of the perpendicular contraction as response to the stretching in one direction for the conservation of volume. This aspect is assumed not to be influencing the center of mass position considerably. The ease of computation is of higher advantage, bringing the sphere to be slightly deformable.

3.6.2 Transition Implementation

The drop mode represents an inherently unstable fluid configuration. When modeling this behavior within a switching-mode system, the transition from drop to the main fluid mass can be handled in different ways. One approach is to track the drop's position: as it approaches the tank walls or the remaining fluid interface, its velocity can be set to zero and its mass reassigned to the main body of fluid. While this method reflects the underlying physics, it introduces sudden changes in inertia and mass, which can complicate the numerical implementation.

An alternative and smoother approach is to model the transition as a gradual change in mass over time. In this case, the drop's mass decreases continuously according to a transition time that depends on the fill ratio. This method avoids abrupt changes in dynamics and better captures the physical process of the drop merging back into the main fluid. Mathematically, the evolution of the drop mass can be expressed as:

$$m_{drop}(t) = \left(1 - \frac{t}{t_{transition}}\right) m_{drop,i} \tag{3.40}$$

This representation ensures that both the motion and the mass of the drop evolve smoothly, preserving numerical stability and maintaining a realistic depiction of the fluid's behavior during the transition.

The transition time can be computed based on some experimental results from [8] and

others as

$$t_s = K \cdot \frac{D^3 \rho}{\sigma}$$

where K can vary in the range of 0.15-0.16 based on different tank shapes, K=0.15 is implemented in the model. For when the velocity of the drop is particularly low, a upper-bound to the duration of the transition could be included. This could be evaluated via CFD results, analysing the overall maximum duration of unstable configurations under low perturbations. Alternatively, to deal with the merging of the drop mass to stable configuration mass, the additional geometric constraint, represented with a smoothed function, can be included in parallel to the time constraint.

Chapter 4

Modes Dynamics and Implementation

To track the evolution of the propellant response inside the tank, it is computationally efficient to define the governing equations of motion and solve them numerically. This approach avoids the need for sensors or cameras inside the tank, although fine-tuning could still benefit from such measurements.

The equations of motion describe how the fluid responds to specific inputs, such as perturbations acting on the tank, gravitational effects at different altitudes, or maneuvering forces from the spacecraft. Since external conditions vary throughout the mission phases, the model representing the fluid's behavior must adapt accordingly. Each of the designed modes is described by its own set of equations of motion, still they all present the same output to ensure the functioning of the following subsystems regardless of the mode that the fluid is in.

Indeed, the Simulink implementation of this model is intended as a component within a larger AOCS simulation environment. In this setup, the sloshing model for a given tank receives inputs from other spacecraft components and simulation modules, including control hardware outputs (forces and angular momentum) as well as external perturbations acting on the spacecraft.

It is also important to note that propellant sloshing is often not the only oscillatory phenomenon coupled to the spacecraft's main structure. Spacecraft may also include features such as double tanks, deployable booms, or large flexible solar arrays. These appendages influence the spacecraft's motion and are themselves affected by it. The

resulting dynamics are coupled between the spacecraft's rotational and translational degrees of freedom and those of the sloshing model (or, similarly, the equivalent models for flexible appendages).

This chapter derives and presents the equations of motion for all three modes of the sloshing model. Firstly considering the two-dimensional case for the ease of the analysis, and then extending to the three-dimensional case - also required for integration into the AOCS simulation. The analysis focuses on representing the tank as an accelerating and rotating frame of known motion, with the fluid's force and torque as outputs and the tank's acceleration and rotation as inputs. Following this structure, the fluid motion is influenced by the motion of the tank but no feedback coupling on the spacecraft dynamics is presented. This framework is considered at least initially due to the alignment with many experimental setups, where tanks are mounted on shakers or gimballed tables with controlled dynamics, and the measurable output is the force on the tank walls.

Finally, the chapter includes the derivation of supporting parameters from available data or known tank characteristics, ensuring that the model can be applied to a variety of spacecraft configurations.

4.1 Equations Mode 1

For sloshing in high-g conditions, the representative model for fluid motion is the pendulum. When subjected to high-magnitude acceleration, the fluid tends to oscillate in the direction of the perturbation with considerably high amplitude. The frequency of oscillation is related to the gravity level and the length of the modeled pendulum, as discussed in Chapter 3. In the literature, the coupling between pendulum motion and spacecraft pitching, as well as the effects of distributed acceleration along different axes, is often neglected. Most common experiments consider high-magnitude acceleration along the z-axis—the longitudinal direction of the tank—with values in the range of $1 - 10, g_0$. In these cases, the equilibrium position of the pendulum aligns with the longitudinal axis of the tank. However, in typical launch or thrusting conditions, the resulting acceleration may not align with any of the body axes, instead forming an angular offset ψ_0 from the vertical.

In the following derivations, based on Landau's theory for a non-inertial frame,

Figure 4.1.1: Mode 1 physical model

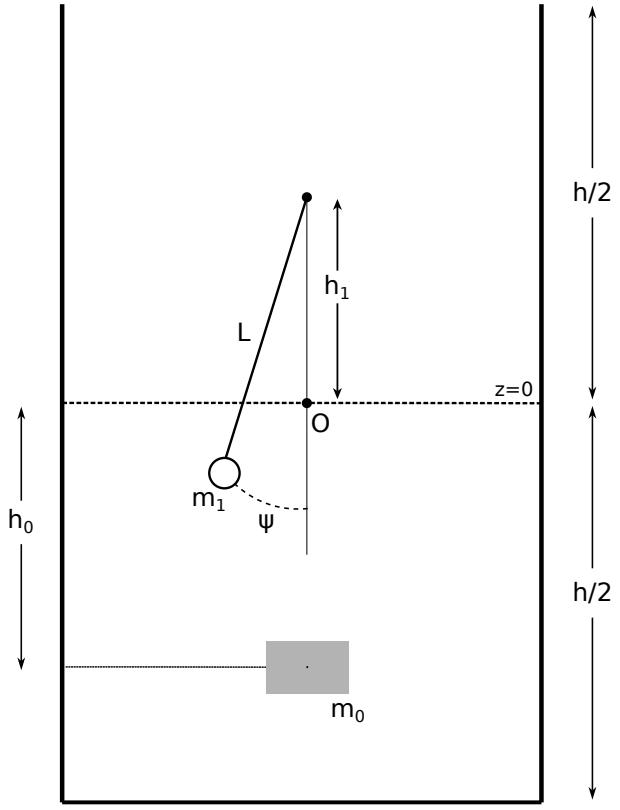

the pendulum is always aligned with the effective acceleration, which includes both thruster and gravitational contributions. Consequently, the bottom of the tank—perpendicular to the equilibrium direction of the pendulum—varies depending on the relative magnitude of the accelerations along the different axes. This holds for any tank shape that is not spherical.

Considering a new equilibrium offset for each possible combination of acceleration components implies that an infinite number of tank orientations would theoretically be needed. Since only part of the fluid is assigned to the pendulum mass, it is important to account for the pendulum rod's equilibrium direction. The remaining fluid mass settles at the bottom of the tank, forming a surface interface perpendicular to the equilibrium direction. Thus, for different orientations, both the bottom configuration and the static fluid shape change, leading to variations in relative mass inertia and center of mass.

Although this aspect is important for modeling, no live function has been implemented to compute the tank shape in high-g conditions based on the experienced accelerations. Practically, two setups can be considered based on the offset angle θ_0. For $\theta_0 \leq 45°$, it is reasonable to assume the tank retains its vertical geometry. For $\theta_0 > 45°$, the tank

geometry can be considered rotated along the perpendicular axis. For instance, an oblate tank may behave as prolate under certain accelerations, while a rectangular tank effectively rotates, flipping its side dimensions. Cylindrical tanks are more complex but can be approximated as rectangular for initial analyses.

The equations of motion are first derived in a 2D projection, considering only the xz plane. Ignoring the feedback interaction with the spacecraft's degrees of freedom, the only free coordinates describe the motion of the included pendulums. When only the first sloshing mode is considered, the dynamics are captured by a single equation, corresponding to the angle of inclination ψ of the pendulum rod relative to the equilibrium position (ψ_0).

The reference frame is centered at the geometric center of the tank, with axes aligned to the tank's body frame.

Considering the Lagrangian for the pendulum, which bob mass is considered inertialess, it results

$$\mathcal{L} = \frac{1}{2}mv^2 + mv \cdot \Omega \times r + \frac{1}{2}m(\Omega \times r)^2 - ma \cdot r - U \tag{4.1}$$

where the vectorial terms are expanded for this configuration as:

- position vector $r = [-Lsin\psi \quad 0 \quad h1 - Lcos\psi]$;
- velocity vector $v = \dot{\psi}[-Lcos\psi \quad 0 \quad Lsin\psi]$;
- frame acceleration $a = [a_x \quad 0 \quad a_z]$;
- frame angular velocity $\Omega = [0 \quad \omega_y \quad 0]$;

while the products $v \cdot \Omega \times r$ and $(\Omega \times r)^2$ result in

$$\begin{aligned}(\vec{\Omega} \times \vec{r})^2 &= [r_z\omega_y \quad 0 \quad -r_x\omega_y] \\ &= [(h1 - Lcos\psi)^2\omega_y^2 \quad 0 \quad L^2cos^2\psi]\end{aligned} \tag{4.2}$$

and

$$\begin{aligned}\vec{v} \cdot \left(\vec{\Omega} \times \vec{r}\right) &= \left[v_x r_z \omega_y \quad 0 \quad -v_z r_x \omega_y\right] \\ &= -\left(h_1 - L\cos\psi\right)\omega_y L\cos\psi\,\dot{\psi} - L^2\sin^2\psi\,\omega_y\,\dot{\psi}\end{aligned} \tag{4.3}$$

Assembling the terms in a scalar way, the resulting Lagrangian is

$$\begin{aligned}\mathcal{L} =&\frac{1}{2}m\dot{\psi}^2(L^2cos^2\psi + L^2sin^2\psi) + m(-(h_1 - Lcos\psi)\omega_y Lcos\psi\dot{\psi}) + mL^2sin^2\psi\dot{\psi} \\ &+ \frac{1}{2}m((h_1 - Lcos\psi)^2\omega_y^2 + L^2sin^2\psi\omega_y^2) + ma_xLsin\psi + ma_z(-h1 + Lsin\psi) - U\end{aligned} \tag{4.4}$$

To derive the EOM forψ, $\mathcal{L}$ need to be derive by the derivative of the generalised coordinate as

$$\frac{d}{dt}\left(\frac{\partial\mathcal{L}}{\partial\dot{\psi}}\right) - \frac{\partial\mathcal{L}}{\partial\psi} = Q_\psi \tag{4.5}$$

$$\frac{\partial\mathcal{L}}{\partial\dot{\psi}} = m\dot{\psi}L^2 - mh_1Lcos\psi\omega_y + mL^2\omega_y \tag{4.6}$$

$$\frac{d}{dt}\left(\frac{\partial\mathcal{L}}{\partial\dot{\psi}}\right) = m\ddot{\psi}L^2 + mh_1L\sin\psi\omega_y\dot{\psi} - mh_1L\cos\psi\dot{\omega}_y + mL^2\dot{\omega}_y \tag{4.7}$$

$$\frac{\partial\mathcal{L}}{\partial\psi} = mh_1\omega_yL\sin\psi\dot{\psi} + mLh_1\sin\psi\omega_y^2 - ma_xL\cos\psi + ma_zL\sin\psi - \frac{\partial U}{\partial\psi} \tag{4.8}$$

The resulting equation of motion describing the evolution of the pedulum bob position, in a tank subjected to acceleration and pitch is

$$\begin{aligned}&mL^2\ddot{\psi} - mh_1\dot{\omega}_yL\cos\psi + \dot{\omega}_ymL^2 - mh_1\sin\psi\omega_y^2 - ma_xLcos\psi \\ &+ ma_zL\sin\psi + m(g_xL\cos\psi + g_zL\sin\psi) = Q_\psi\end{aligned} \tag{4.9}$$

Where as potential expression has been added the gravitational influence with its components on the xz plane. When the spacecraft is not aligned with the direction of the gravitational field, it is not possible to consider gravity only acting on its longitudinal axis, but instead it needs to get decomposed on projections on the body frame axis. Given a model in the inertial frame representing the gravity gradient, with the known rotation matrix R_{BI} from inertial to body frame, it is possible to input the right components.

As generalised forces applied on the system, some disturbances can be added, also expressed in body frame coordinates. Here the term Q_ψ can include also the expression for dissipation, which cannot be added in the classic Lagrangian. In particular, from

the derivations explained in Chapter 3, the damping coefficient is included as

$$Q_{psi} = -c\dot{\psi} \tag{4.10}$$

where c is a coefficient based on the damping ratio ζ and shaped to contribute as angular dissipative term.

This equation is implemented in the Simulink model under the Mode 1 block. It describes the position of the pendulum mass in the body frame, which is always aligned with the effective acceleration vector.

In this formulation, the tank motion is considered known and is not coupled back to the sloshing motion. When full coupling between the pendulum and the spacecraft/tank motion is considered, x_B and z_B also become degrees of freedom, representing the translations along the body x and z axes, respectively. Additionally, pitching is treated as a generalized coordinate, denoted by θ.

The setup differs slightly because the tank motion no longer appears as pseudo-forces acting on the internal motion. The velocity vector must now be expanded to include all terms that cannot be neglected (see Landau's derivation for an accelerating frame in[17]).

Velocity is defined both for the pendulum mass and for the static mass. The static mass is referenced to the tank center and added to the static fluid mass, denoted as M. The inertia I_B is also assumed to be referenced to the tank center. For the fluid mass, this is straightforward, while for the remaining spacecraft mass, the parallel axis theorem must be applied twice in this setup.

The pendulum velocity is then:

$$v_{pend} = \vec{v_B} + \frac{d\vec{r}}{dt} + \vec{\Omega} \times \vec{r} \tag{4.11}$$

The resulting Lagrangian for the fully coupled dynamics is computed as

$$\begin{aligned}\mathcal{L} = &\frac{1}{2}m\dot{\psi}^2L^2 + m\dot{\psi}((-h_1 + Lcos\psi)\omega_y Lcos\psi) + mL^2sin^2\psi\omega_y\dot{\psi} \\ &+ \frac{1}{2}m(h_1 - Lcos\psi)^2\omega_y^2 + \frac{1}{2}mL^2sin^2\psi\omega_y^2 + mLa_xsin\psi + \\ &- ma_zh_1 + ma_zLcos\psi - U_{pend} + \frac{1}{2}M(\dot{x_B}^2 + \dot{z_B}^2) + \frac{1}{2}\dot{\theta}^2I_B - U_B\end{aligned} \tag{4.12}$$

With some derivation in the same fashion as the equation derived above, the resulting dynamics of the coupled motion are the following four:

- pendulum angle ψ:

$$\begin{aligned} m\ddot{\psi}L^2 = &-mL^2\ddot{\theta} + mh_1\ddot{\theta}Lcos\psi + mh_1\dot{\theta}^2Lsin\psi + mLcos\psi(\ddot{x}_B + \dot{z}_B\dot{\theta}) + \\ &- mLsin\psi(\ddot{z}_B - \dot{x}_B\dot{\theta}) - \frac{\partial U_{pend}}{\partial \psi} - \frac{\partial U_B}{\partial \psi} + Q_\psi \end{aligned} \tag{4.13}$$

- body traslation on x axis x_B:

$$\begin{aligned} (M+m)\ddot{x}_B = &-\dot{\psi}^2mLsin\psi + \ddot{\psi}mLcos\psi - m\ddot{\theta}(h_1 - Lcos\psi) - m\dot{\psi}\dot{\theta}Lsin\psi + \\ &- \frac{\partial U_{pend}}{\partial x_B} - \frac{\partial U_B}{\partial x_B} + Q_{B_x} \end{aligned} \tag{4.14}$$

- body traslation on z axis z_B:

$$\begin{aligned} (m+M)\ddot{z}_B = &\dot{\psi}^2mLcos\psi - \ddot{\psi}mLsin\psi - \ddot{\theta}mLsin\psi - \dot{\psi}m\dot{\theta}Lcos\psi + \\ &- \frac{\partial U_{pend}}{\partial z_B} - \frac{\partial U_B}{\partial z_B} + Q_{z_B} \end{aligned} \tag{4.15}$$

- rotation of the body θ:

$$\begin{aligned} \ddot{\theta}(I_B + mL^2 + mh_1^2 - 2mh_1Lcos\psi) = &\ddot{\psi}(mL^2 - mh_1Lcos\psi) - \dot{\psi}^2mh_1Lsin\psi + \\ &- 2\dot{\psi}mh_1Lsin\psi\dot{\theta} - mLcos\psi(-\ddot{x}_B + \dot{z_B}\dot{\psi}) + \\ &- \ddot{x}_Bh_1m - mLsin\psi(\dot{x}_B\dot{\psi} + \ddot{z}_B) + Q_\theta + \\ &- \frac{\partial U_{pend}}{\partial \theta} - \frac{\partial U_B}{\partial \theta} \end{aligned} \tag{4.16}$$

In these derivation the generalised forces Q_i can be inserted as also damping on different DOF. Although here only the sloshing damping is relevant. Other forces and torques that can fall under this description are the forces from the thrusters or the torques from reaction wheels using for maneuvres. In this case the right handling of these terms is through virtual work and respective generalised force acting on the correct system component. For a thrust or a torque given in body frame, the virtual

work is

$$\delta W = \vec{F} \cdot \delta r_T + \vec{\tau} \delta \phi \tag{4.17}$$

The respective generalised force for a force acting only at the tank center is

$$Q_i = \vec{F} \cdot \frac{\partial \vec{r_{tank}}}{\partial q_i} \tag{4.18}$$

and for a force acting at the hinge of the pendulum is

$$Q_i = \vec{F} \cdot \frac{\partial \vec{r_{tank}}}{\partial q_i} + \vec{F} \cdot \frac{\partial \vec{r_{pend}}}{\partial q_i} \tag{4.19}$$

The same approach applies to generalized torques. In this way, the control action applied through hardware enters directly into the equations of motion, making it possible to monitor the evolution of the fluid motion for any control input received.

When extending the model to three-dimensional motion, it is useful to describe the possible alternatives. The fluid responds to lateral motion with perturbations confined to the plane of the applied force. Therefore, a fluid receiving an input along any axis will tend to oscillate and eventually damp only along that axis. It is physically justified to consider planar motion when a disturbance is received. Aligning the main thruster with the fixed reference frame simplifies the analysis; otherwise, a rotation matrix can be used to align the thrusting or torquing axis with the tank axes. Off-plane fluid motion, referred to as swirling, is induced by a periodic lateral disturbance with the same frequency as the slosh natural frequency. For this initial model, this motion can be neglected. An alternative is to model the fluid as a spherical pendulum, which is inherently three-dimensional but results in much more complex equations when coupled with spacecraft motion.

To achieve a computationally lighter and physically intuitive model while retaining dynamic accuracy, a double-plane assembly is used for three-dimensional fluid motion. Specifically, the pendulum motion in the xz plane, excited by pitch and acceleration, is paired with an equivalent model in the yz plane. In this setup, the degrees of freedom for high-g sloshing, when fully coupled with the spacecraft motion, are: [x_B,y_B,z_B,θ_x,θ_y,ψ_x ,ψ_y]. The spinning motion of the longitudinal direction (θ_z) of the tank is modelled separately. It becomes relevant for motions typical of the first phases of a mission,as launch and despun.

Figure 4.1.2: 3D set up-z coordinate constraint

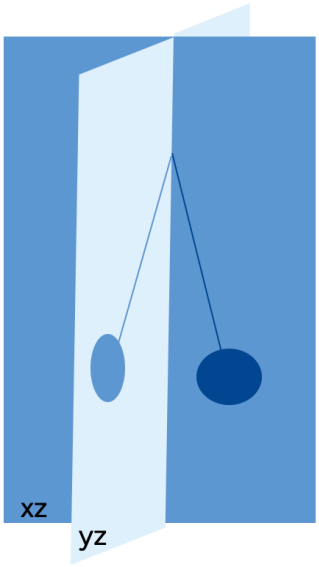

In this configuration, the same pendulum model is used on both planes. The pendulum position in each plane is:

$$r_{pend_{xz}} = \begin{bmatrix} -Lsin\psi_x & 0 & h1 - Lcos\psi_x \end{bmatrix} r_{pend_{yz}} = \begin{bmatrix} 0 & -Lsin\psi_y & h1 - Lcos\psi_y \end{bmatrix} \tag{4.20}$$

From these vectors, it is evident that the z component is computed in the same way in both planes but depends on different angles. The two expressions cannot be treated independently. Therefore, only the lateral components x and y are used from each plane in the three-dimensional model.Instead, the vertical component z must be recomputed as a function of both angles to satisfy the physical constraint of a rigid pendulum rod.

The $z(\psi_x, \psi_y)$ component can be derived from the pendulum length L derived as:

$$(x_{pend}(\psi_x))^2 + (y_{pend}(\psi_y))^2 + (h1 - z(\psi_x, \psi_y))^2 = L^2 \tag{4.21}$$

and z results from the nonlinear expression

$$z(\psi_x, \psi_y) = h1 - \sqrt{L^2 - x_{pend}(\psi_x)^2 - y_{pend}(\psi_y)^2} \tag{4.22}$$

that when the component $y_p = 0$ results $z = h1 - \sqrt{L^2 - x_{pend}^2} = h1 - Lcos\psi_x$

To finilise the computation and write the correct Lagrangian the pendulum mass

velocity $\frac{dr_{pend}}{dt}$ becomes:

$$r_{pend} = \begin{bmatrix} -Lsin\psi_x & -Lsin\psi_y & h1 - \sqrt{L^2 + (Lsin\psi_x)^2 + (Lsin\psi_y)^2} \end{bmatrix} \tag{4.23}$$

$$\begin{aligned} v_{pend} &= \frac{dr_{pend}}{dt} \\ &= \begin{bmatrix} -\dot{\psi_x} Lcos\psi_x & -\dot{\psi_y} cos\psi_y & (-\frac{Lsin\psi_x \cdot (\dot{\psi_x} cos\psi_x)}{\sqrt{L^2+(Lsin\psi_x)^2+(Lsin\psi_y)^2}} - \frac{Lsin\psi_y \cdot (\dot{\psi_y} Lcos\psi_y)}{\sqrt{L^2+(Lsin\psi_x)^2+(Lsin\psi_y)^2}}) \end{bmatrix} \end{aligned} \tag{4.24}$$

This velocity component of the pendulum mass must be combined with the tank velocity and the contribution from tank rotation.The Lagrangian of the coupled system becomes:

$$\mathcal{L} = \frac{1}{2} m(\vec{v}_{pend} + \vec{v}_B + \vec{\Omega} \times \vec{r}_{pend})^2 + \frac{1}{2} M \vec{v}_B^2 + \frac{1}{2} \vec{\Omega} I_B \vec{\Omega} - V_{pend} - V_B \tag{4.25}$$

This mode represents the oscillation of a fluid under high magnitude accelerations. This condition is characterised by high amplitude oscillations and, potentially, important and abrupt changes of direction of a_{eff}. For this reason, the dynamics of the pendulum cannot be linearised. Models found in literature -mostly linear- do not provide coverage for cases where the direction of the acceleration vector varies in the time evaluated, while, for this kind of application, this aspect must be considered. Moreover, the mass oscillating under external inputs can provide high torque and forces coupled with the spacecraft, also due to the great displacement. For this reason, the pendulum model has been kept as abstract parametrization of this movement, trying to fit it to the complete scenario of external disturbances with no assumption of small angle approximation validity. The physical constraint of the tank walls plays a role in the motion of the mass, especially if referred to the pendulum rod length. However, as already mentioned in the previous chapter, as first approximation, the influence of tank walls is assumed not relevant. This is especially valid due to the higher amplitude that characterises lower filling ratio scenarios, to which correspond also shorter equivalent pendulum rods.

4.2 Equations Mode 2

In low-g conditions, which are reached at different stages depending on tank dimensions and fill ratio, the fluid is modeled as clinging to the walls of the tank. The

Figure 4.2.1: Mode 2 physical model, cross section view

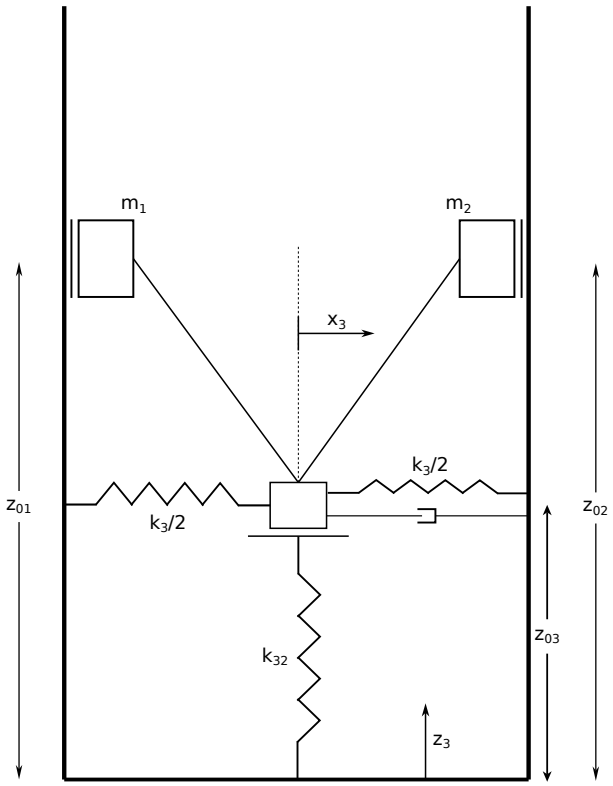

assumption in this model is that the fluid orientation in the tank can be inferred from previously experienced high-g sloshing. Specifically, the position of the pendulum mass from the high-g model is passed to the low-g model to define the fluid mass location. Infact, the position stored of the mass woudl get passed to the model for capillarity, and there the mass would be based. The available orientations are horizontal or vertical sides of the tank, with opposite directions. For pendulum angles within $-45° < \psi < 45° || -135° < \psi < 135°$ the capillarity model is applied along the longitudinal direction of the tank. Outside this range, the perpendicular geometry is used, according to the guidelines presented earlier.

This approach requires, for each tank under analysis, the identification of configuration parameters and the implementation of a memory block and switching logic to determine which model to use at each transition.

Compared to the pendulum model, the low-g model demands greater attention to tank geometry and careful handling of different fill ratios, especially for curved tanks.

A planar representation of the capillarity effect on fluid contains three masses,as in Figure4.2.1. These masses are connected to each other to physically represent the surface tension of the fluid and its resistance to separation. All these three masses have

position and velocity vectors which contribute to the total Lagrangian. However, the degrees of freedom are only two:x_3 and z_3. The other masses have dynamics constraint to m_3 motion. From geometric relationships, it is evident that once z_{01} and z_{02} are known the vertical motion of the lateral masses stands to

$$(z_{01}^2 + (\frac{D}{2} + x_3)^2) = d^2 = \text{const} \tag{4.26}$$

or in other terms using one DOF for each lateral mass

$$\begin{aligned} z_i &= dsin\theta_i \\ x_3 &= \frac{D}{2} - dcos\theta_2 = dcos\theta_1 \end{aligned} \tag{4.27}$$

implying $\theta_2 = acos(\frac{-dcos\theta_1 + \frac{D}{2}}{d})$.

In either way the constraint of the rigid rod is maintained, describing the coupled up-and-down motion of the lateral masses. The nonlinearities derived can become difficult to handle in the derivation, due to much more complex chained rule terms. Moreover, the system is not easily tunable for different fill ratios. It is relevant to relax the rigid rod constraint to include in the model a tunable parameter that represents the difference in height reached by the fluid in high fill ratio and low fill ratios, where the fluid clings even more.

For this reason a new parameter α is introduced. It is shaped to create the mathematical constraint between variables, maintaining x_3 and z_3 the only degrees of freedom and it is a linear function of the fill ratio. In particular, it can be expressed as

$$\alpha(fill_r) - \alpha_0(1 - fill_r) \tag{4.28}$$

where α_0 is derived based on

$$\begin{aligned} z_1 &= z_3 + \sqrt{d^2 - (x_3 + D/2)^2} \\ \frac{dz_1}{dx_3}\Big|_{x_3=0} &= \frac{x_3 + D/2}{\sqrt{d^2 - (x_3 + D/2)^2}}\Big|_{x_3=0} \\ &= \frac{D/2}{\sqrt{d^2 - D^2/4}} \end{aligned} \tag{4.29}$$

and d can be expressed as $\sqrt{D^2/4 + z_{01}^2}$, resulting in the defining equation function of

all known terms, from geometry of the tank and parameters computation as in

$$\alpha_0 = \frac{\sqrt{D^2/4 + z_{01}^2}}{z_{01}} \tag{4.30}$$

The horizontal component of the position vector of the model in xz plane is instead based on geometry only. Taking the width of the tank, constant or varying with fill ratio, at the fluid height before computing the curvature height, the position of the lateral masses on the x axis is $x_{01} = -\frac{1}{3}D$ and $x_{02} = +\frac{1}{3}D$. While the vertical position, for what derived above, is:

$$\begin{aligned} z_1 &= z_{01} - \alpha \cdot x_3 + z_3 + z_{03} \\ z_2 &= z_{02} + \alpha \cdot x_3 + z_3 + z_{03} \end{aligned} \tag{4.31}$$

The position vectors become:

- position m_1: $r_1 = [-\frac{D}{3} \quad 0 \quad z_{01} - \alpha \cdot x_3 + z_3 + z_{03}]$;
- position m_2: $r_2 = [\frac{D}{3} \quad 0 \quad z_{02} + \alpha \cdot x_3 + z_3 + z_{03}]$;
- position m_3:$r_3 = [x_3 \quad 0 \quad z_{03} + z_3]$;

The respective velocity vectors are:

- velocity m_1 :$v_1 = [0 \quad 0 \quad \dot{z}_3 - \alpha\dot{x}_3]$;
- velocity m_2:$v_2 = [0 \quad 0 \quad \dot{z}_3 + \alpha\dot{x}_3]$;
- velocity m_3: $v_3 = [\dot{x}_3 \quad 0\dot{z}_3]$;

To derive the equation of motion describing the evolution of the dynamics of the three masses in low-g, Landau derivation is used as in the section above. Simply, in this model the formalism is applied to all the three masses and it will present additional terms of potential energy given by the two springs. This mechanical addition serves to keep into consideration the oscillating motion of the fluid but also its intrinsically elastic energy. The Lagrangian for this model, when the tank is considered the

accelerated frame and no full coupling is considered is:

$$\begin{aligned}\mathcal{L} =&\frac{1}{2}m_1(\vec{v_1}^2 + (\vec{\Omega}\times\vec{r}_1)^2 + 2\vec{v_1}\cdot\vec{\Omega}\times\vec{r}_1) + \frac{1}{2}m_2(\vec{v_2}^2 + (\vec{\Omega}\times\vec{r}_2)^2 + 2\vec{v_2}\cdot\vec{\Omega}\times\vec{r}_2)+\\ &+\frac{1}{2}m_3(\vec{v_3}^2 + (\vec{\Omega}\times\vec{r}_3)^2 + 2\vec{v_3}\cdot\vec{\Omega}\times\vec{r}_3) - m_1\vec{a}\cdot\vec{r_1} - m_2\vec{a}\cdot\vec{r_2} - m_3\vec{a}\cdot\vec{r_3}+\\ &-\frac{1}{2}k_{31}x_3^2 - \frac{1}{2}k_{32}z_3^2 - V_1 - V_2 - V_3\end{aligned} \tag{4.32}$$

Where the potential contribution on each mass can be added under the relative V_i. However, for the conditions for which this model is assumed relevant, the gravitational potential can be neglected.

When developing the products of vector, the Lagrangian in scalar components is

$$\begin{aligned}\mathcal{L} =&\frac{1}{2}m_1(\dot{z}_3^2 + \alpha^2\dot{x}_3^2 - 2\alpha\dot{x}_3\dot{z}_3 + \omega_y^2(z_{03} + z_3 - \alpha x_3 + z_{01})^2 + \omega_y^2 x_{01}^2 + 2(\dot{z}_3 - \alpha\dot{x}_3)(-x_{01}\omega_y))+\\ &+\frac{1}{2}m_2(\dot{z}_3^2 + \alpha^2\dot{x}_3^2 + 2\alpha\dot{x}_3\dot{z}_3 + \omega_y^2(z_{03} + z_3 + \alpha x_3 + z_{02})^2 + \omega_y^2 x_{02}^2 + 2(\dot{z}_3 - \alpha\dot{x}_3)(-x_{02}\omega_y))+\\ &+\frac{1}{2}m_3(\dot{x}_3^2 + \dot{z}_3^2 + \omega_y^2(z_{03} + z_3)^2 + \omega_y^2 x_3^2 + 2\dot{x}_3\omega_y(z_{03} + z_3) - 2\dot{z}_3\omega_y x_3)+\\ &-m_1a_{B_x}x_{01} - m_1a_{B_z}(z_{03} - \alpha x_3 + z_{01} + z_3) - m_2a_{B_x}x_{02} - m_2a_{B_z}(z_{03} + \alpha x_3 + z_{02} + z_3)+\\ &-m_3a_{B_x}x_3 - m_3a_{B_z}(z_3 + z_{03}) - \frac{1}{2}k_{31}x_3^2 - \frac{1}{2}k_{32}z_3^2\end{aligned} \tag{4.33}$$

After proceeding in the Lagrangian derivation and applying $m_1 = m_2 = m$, they result as:

$$\begin{aligned}\ddot{x}_3(2m\alpha^2 + m_3) =& -\alpha\dot{\omega}_y(x_{01} + x_{02}) - m_3\dot{\omega}_y(z_{03} + z_3) - m_3\omega_y\dot{z}_3 - m_3a_{B_x}+\\ &+m_3\omega_y^2x_3 - m_3\dot{z}_3\omega_y - k_3x_3 + m\omega_y^2\alpha(2z_{03} + 2z_3 + z_{01} + z_{02})\end{aligned} \tag{4.34}$$

$$\begin{aligned}\ddot{z}_3(2m + m_3) =& m\dot{\omega}_y(x_{01} + x_{02}) + m_3\dot{\omega}_y z_3 + m_3\omega_y\dot{z}_3 - a_{B_z}(2m + m_3)+\\ &+m_3\omega_y^2(z_{03} + z_3) + m_3\dot{x_3}\omega_y - k_{32}z_3 + m\omega_y^2(2z_{03} + 2z_3 + z_{01} + z_{02})\end{aligned} \tag{4.35}$$

When working in three dimensional environments the model gets slighlty more complex in its set up. The shape of the equations remains the same but with few added terms that make it a bit lenghty but with easy derivations. The 3D design can be observed in Figures

The masses are now five, since the central mass which mimics the water under the

Figure 4.2.2: Mode 2 3D model

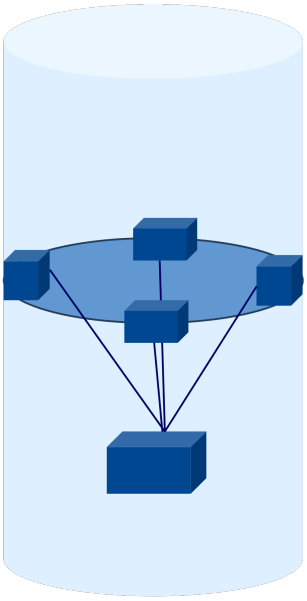

Figure 4.2.3: Mode 2 top view, rods here are omitted for clarity

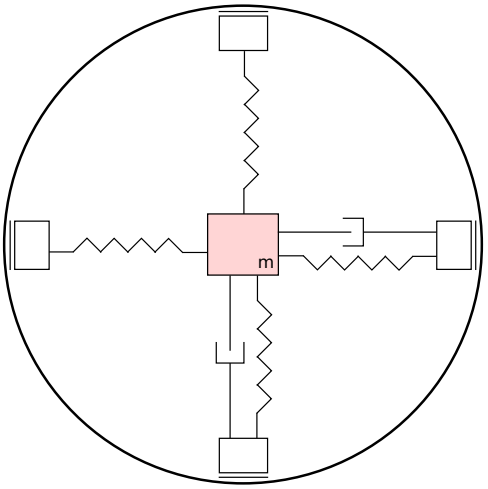

meniscus is still represented as m_3. The raise of the fluid is now represented on all body axes as approximation of the continuity of the fluid on the walls. The position vectors are now:

- $\vec{r_1} = [x_{01} \quad y_3 \quad z_{03} + z_{01} + z_3 - \alpha x_3]$
- $\vec{r_2} = [x_{02} \quad y_3 \quad z_{03} + z_{02} + z_3 + \alpha x_3]$
- $\vec{r_3} = [x_3 \quad y_3 \quad z_3 + z_{03}]$
- $\vec{r_4} = [x_3 \quad y_0 4 \quad z_{03} + z_3 + z_{04} - \beta y_3]$
- $\vec{r_5} = [x_3 \quad y_0 5 \quad z_{03} + z_3 + z_{05} + \beta y_3]$

Where the new parameter β is defined exactly like α but can present another value for β_0 due to different geometry of the cross section of the tank in the yz plane. The intrinsic velocity vector of the masses inside of the tank, without considering the contribution of the frame motion are:

- $\vec{v}_1 = [0 \quad \dot{y}_3 \quad \dot{z}_3 - \alpha\dot{x}_3]$
- $\vec{v}_2 = [0 \quad \dot{y}_3 \quad \dot{z}_3 + \alpha\dot{x}_3]$
- $\vec{v}_3 = [\dot{x}_3 \quad \dot{y}_3 \quad \dot{z}_3]$
- $\vec{v}_4 = [\vec{x}_3 \quad 0 \quad \dot{z}_3 - \beta\dot{y}_3]$
- $\vec{v}_5 = [\vec{x}_3 \quad 0 \quad \dot{z}_3 + \beta\dot{y}_3]$

The 3D Lagrangian fully coupled is:

$$\mathcal{L} = \Sigma_{i=1}^{n=5}\frac{1}{2}m_i(\vec{v}_i + \vec{v}_B + \vec{\Omega}\times\vec{r}_i)^2 + \frac{1}{2}M\vec{v_B}^2 + \frac{1}{2}\vec{\Omega}^T I_B\vec{\Omega} - (\frac{1}{2}k_3x_3^2 + \frac{1}{2}k_3y_3^2\frac{1}{2}k_{32}z_3^2) - U_i - U_B \tag{4.36}$$

The possibility to slide horizontally of the lateral masses is allowed due to the small amplitude oscillations in low gravity conditions. Indeed this assumption holds for the same conditions the capillarity mode in employed. For rectangular shapes this has no assumptions needed, for vertical cylinders and oblate shaped this assumes that the horizontal movement of the lateral masses follows a straight trajectory for the small displacements.

4.3 Equations Mode 3

The bubble configuration models part of the unstable configurations that a fluid,or a portion of it, can assume during transitions or under extremely low-g conditions when subjected to small perturbations. The setup is conceptually simple and is illustrated in Figure4.3.1.

Resting on springs, the fluid blob is held approximately at the center of the tank, free to move under small perturbations. Its dynamics are dominated by surface tension effects, which govern oscillations. The spring constants and the resulting mass dynamics are therefore determined entirely by the capillarity of the fluid interface.

Figure 4.3.1: Mode 3 physical model, planar

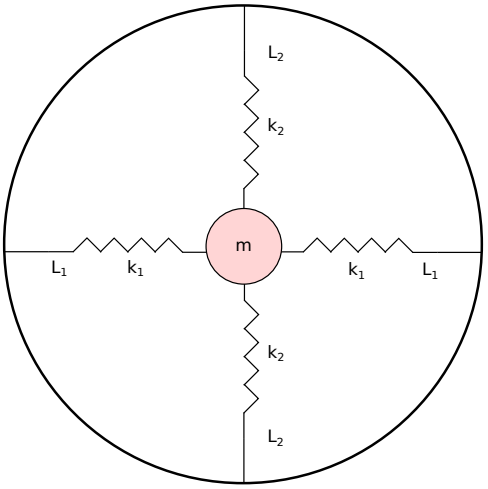

Tracking the dynamics of this mass is important for simulation purposes, both to monitor the motion of a coherent portion of the fluid and to estimate behavior during transition times. The duration in which the drop mode is active corresponds to the transition time defined in Chapter 3

Considering motion in the xz-plane, the position and velocity vectors of the drop are

- $r_{drop} = [x \quad 0 \quad z]$;
- $v_{drop} = [\dot{x} \quad 0 \quad \dot{z}]$;

These vectors correctly represent the free movement of the drop inside the tank.

The contribution of surface tension is represented via springs connecting the drop to the tank walls (center, bottom, and top). The deformation of each spring is computed using the Pythagorean theorem, as the spring stretches or compresses when the drop moves from the equilibrium center.

The elastic potential energy of a spring is proportional to the square of its deformation. For a perturbed configuration, where the mass is displaced from the tank center, the spring lengths can be computed as:

- $\Delta l_1 = \sqrt{(L_{01} - z)^2 + x^2} - L_{01}$;
- $\Delta l_2 = \sqrt{(L_{02} - x)^2 + z^2} - L_{02}$;
- $\Delta l_3 = \sqrt{(L_{01} + z)^2 + x^2} - L_{01}$;
- $\Delta l_4 = \sqrt{(L_{02} + x)^2 + z^2} - L_{02}$

When these expressions are considered in the full Lagrangian for the derivation of the EOM of the drop the expression results:

$$\begin{aligned}\mathcal{L} = &\frac{1}{2}m(\dot{x}^2 + \dot{z}^2 + \omega^2 z^2 + \omega_y^2 x^2 + 2\omega_y z\dot{x} - 2\omega_y \dot{z}x) - ma_{B_x}x - ma_{B_z}z + \\ &- \frac{1}{2}k\big((\sqrt{(L_{01}-z)^2 + x^2} - L_{01})^2 + (\sqrt{(L_{02}-x)^2 + z^2} - L_{02})^2 + \\ &+ (\sqrt{(L_{01}+z)^2 + x^2} - L_{01})^2 + (\sqrt{(L_{02}+x)^2 + z^2} - L_{02})^2\big)\end{aligned} \tag{4.37}$$

The derivation above describes the dynamics as stable in the ceter with forces pulling from different direction and anchor-points. The EOM for this model are:

$$\begin{aligned}m\ddot{x} = &-m\omega_y\dot{z} - mz\dot{\omega}_y + mx\omega_y^2 + m\omega_y\dot{z} - ma_{B_x} - 4kx + \frac{kxL_{01}}{\sqrt{(L_{01}-z)^2 + x^2}} + \\ &- \frac{kL_{02}(L_{02}-x)}{\sqrt{(L_{02}-x)^2 + z^2}} + \frac{kL_{01}x}{\sqrt{(L_{01}+z)^2 + x^2}} + \frac{kL_{02}(L_{02}+x)}{\sqrt{(L_{02}+x)^2 + z^2}} + Q_x\end{aligned} \tag{4.38}$$

$$\begin{aligned}m\ddot{z} = &\, m\omega_y\dot{x} + m\dot{\omega}_y x + m\omega_y^2 z + m\omega_y\dot{x} - ma_{B_z} - 4kz - \frac{kL_{01}(L_{01}-z)}{\sqrt{(L_{01}-z)^2 + x^2}} \\ &+ \frac{kL_{02}z}{\sqrt{(L_{02}-x)^2 + z^2}} + \frac{kL_{01}(L_{01}+z)}{\sqrt{(L_{01}+z)^2 + x^2}} + \frac{kL_{02}z}{\sqrt{(L_{02}+x)^2 + z^2}} + Q_z\end{aligned} \tag{4.39}$$

However, the assumption of fixed spring can be relaxed as explained in the previous chapter, with the model still remaining a suitable representation of the physical model. In fact, both model have been derived, so that with the verification of the results can highlight the eventual differences - however, there are believed to be minimal. When the springs are put on skids able to slide on the walls and be deformed only longitudinally, the equation simplify considerably. This is valuable especially for the fully coupled three dimensional case but it can be seen already in the 2D derivation presented here below. When the deformations become simply:$\Delta l_1 = \Delta l_3 = x$ and $\Delta l_2 = \Delta l_4 = z$, the governing equations become

$$m\ddot{x} = -m\dot{\omega}_y z - m\omega_y\dot{z} + m\omega_y^2 x - m\omega_y\dot{z} - ma_{B_x} - 2kx + Q_x \tag{4.40}$$

$$m\ddot{z} = +m\dot{\omega}_y x + m\omega_y\dot{x} + m\omega_y^2 z + m\omega_y\dot{x} - ma_{B_x} - 2kz + Q_z \tag{4.41}$$

When the three dimensional model is needed the previous equation adapt easily to form the needed Lagrangian. It is important to notice that, differently from Mode 2, the mass is not divided differently in the 2D setup than the 3D ones. What changes are

the number of springs considered that pass from being four to being six, two on each axis.

Therefore the fully coupled Lagrangian in 3D is:

$$\mathcal{L} = \frac{1}{2} m_{drop}(\vec{v}_{drop} + \vec{v}_B + \vec{\Omega} \times \vec{r})^2 + \frac{1}{2} M \vec{v_B}^2 + \frac{1}{2} \vec{\Omega}^T I_B \vec{\Omega} - k(x^2 + y^2 + z^2) - U_B - U_{drop} \quad (4.42)$$

U_B could contain also gravitational contribution which might be disregarded here as well. In U_{drop} some component of surface potential energy can be included. It is important to acknowledge that part of the surface tension effects are already embedded in the spring nature which is itself based on the elastic properties of the drop.

4.4 Switching Logic

The switching logic is modified from the blunt switch based on Bond number thresholds. Instead, in a continuous way, some parameters, the weight functions, are computed for every fill ratio and input condition which are shaped to compute the relative dominance of each mode for every condition. The weights for each of the three mode can vary from 0 to 1. This means that in 'mode dominance' ranges for both the stable modes, the relative weight of the representative dominant mode will be computed as 1 and for the other two modes the weight will be 0. During transition these weight are more varied. The transition, which is a unstable mode with computed duration (transition time t_{trans}) comprehends all the modes at once, until the drop mode is absorbed in one of the two stable modes with a function of time. A new stable mode in included: this has a similar shape to the transitory configuration but it does not have a limited time of actuation. It considered all the three modes at once and aims to represent the range between Mode 1 and Mode 2 thresholds, where the dynamics is not obeying to any specific mode.

4.5 Generalised Use

For the implementation of sloshing in a spacecraft with multiple tanks or other flexible subsystems, the modeling approach presented in this thesis remains valid. In particular, the method used to compute the dynamics allows for full coupling between the spacecraft and the fluid, even though the resulting differential equations

are nonlinear. Each subsystem i can be described by its own equivalent mass and other matrices, $M^{(i)}(q^{(i)}), C^{(i)}(q^{(i)}, \dot{q}^{(i)}), G^{(i)}(q^{(i)})$, as well as generalized forces $Q^{(i)}(t)$. The matrix C can be directly associated to terms as Coriolis force, depending on the system velocity, while the matrix G contains terms depending on the system position vector. These can be assembled into a global system:

$$\underbrace{\sum_i M^{(i)}(q)}_{\text{global mass matrix}} \ddot{q} + \underbrace{\sum_i C^{(i)}(q,\dot{q})}_{\text{global Coriolis/centrifugal type forces}} \dot{q} + \underbrace{\sum_i G^{(i)}(q)}_{\text{global conservative forces}} = \underbrace{\sum_i Q^{(i)}(t)}_{\text{global generalized forces}} \tag{4.43}$$

where q is the global vector of degrees of freedom including all subsystems.

Within the Lagrange-d'Alembert principle, all non-potential effects can be introduced as generalized forces and be collected into a function

$$Q_{\text{nc}} : (q, \dot{q}, t) \mapsto \mathbb{R}^n,$$

so that the equations of motion become

$$M(q)\,\ddot{q} + C(q,\dot{q})\,\dot{q} + g(q) = Q_{\text{ext}}(t) + Q_{\text{nc}}(q,\dot{q},t).$$

This term includes the following contributions:

$$Q_D(q,\dot{q}) = -D(q)\,\dot{q}, \quad \text{viscous/Rayleigh damping, derived from } R(q,\dot{q}) = \tfrac{1}{2}\,\dot{q}^\top D(q)\dot{q},$$

$$Q_{\text{ext}}(t) = u(t), \qquad \text{external inputs, control, or disturbances.}$$

and potential other terms with general nonlinearities functions of ($\dot{q}_i$,q_i). This formulation allows additional oscillating components to be incorporated naturally: each new subsystem contributes its own matrices to the total system, preserving the full coupling between spacecraft and all flexible or fluid elements.

Chapter 5

Model Description and User Guide

The theory presented in the previous chapters shapes a relative Simulink model, which this thesis has shaped in an initial form. This chapter aims to give a structure guideline for a reader of the model. Here, all the derivation are explained in their applications and the model created is described in its structure and its inputs and outputs.

The AOCS model that this thesis research for, was aimed to interface the slosh model with an already coupled system, where the spacecraft had added dynamical terms from control hardware, solar array or other structures.

The results found in the previous chapter create the base and the theory to shape a model which is adaptable to different fluid, tank shapes(rectangular, cylindrical, spherical and oblate(prolate)), tank dimensions, filling ratio and mission phase.

For this reason, some inputs and parameters need to be described before running the model describing the switching condition and the dynamics of the modes. In particular, in this chapter the ”general conditions” are going to be introduced as used in the model.

5.1 Fluid Parameters

The propellant used in the tank can be different, and few parameters describe its nature impact on the motion. In particular, in a file of variables initialization, the fluid density ρ and the fluid tension σ need to be set. For the current model, the dynamics is based on a fixed value of contact angle θ_c which is taken as $\theta_c = 0$, which is found to be accurate for common space propellants[**NASA_Cold-sat**][8]. If its precise value is available,

it can be directly included in the formula of the Bond number as by definition. The presented parameters enters as workspace variables computed at the beginning of the simulation.

5.2 Tank Shape and Dimension

The tank shapes are labeled with a numbered constant that identifies Rectangular shape with ”shape=1”, Cylindrical shape with ”shape=2”, and Oblate shape with ”shape=3”. All the parameters for spherical tanks are also derived but not yet included in the files’ structure. The characteristic dimension of the tank is also needed with the current inertia computation block, and can be set in the same file. Throughout the proposed model structure, conditional blocks compute the needed parameters based on the shape set at the beginning of the simulation.

Moreover, the functions found in Chapter 3 describing the evolution of parameters for different tank shapes should be included in the Matlab function block of ”parameters computation” which includes COM displacement and total propellant mass in the current model. The last term is a linear decrease of the propellant with fill ratio that can be easily shaped for any needed condition.

The `MAIN` file calls `generate_fluid_tank_param`, where the dimensions and the volume of the tank are set in a switch case based on the shape description label. Here, the fluid height parameter is computed as time-series with an approximation. The file should be integrated with the resulting relation linking fluid height and fill ratio as in Chapter 3 3.18.

The shape-dependent parameters for Mode 2 and Mode 3 are dynamically computed based on the variable `shape` within the model. For Mode 3, parameters such as spring lengths are directly evaluated within the corresponding enabled subsystems. More complex is the initialization of the Mode 2 masses’ positions, which depends on both the fill ratio and the tank geometry and therefore needs to be calculated during the simulation run-time. Within the Mode 2 enabled subsystem, the MATLAB function `mode2_get_param` computes the equivalent mechanical parameters of a fluid under microgravity conditions as a function of the tank geometry and the fill ratio. Its inputs include the total fluid mass m_{tot}, the apparent acceleration vector $\mathbf{a}_B$, the liquid height h, a geometry selection parameter (`caso`, distinguishing between

rectangular,cylindrical and oblate tanks), and the fill ratio f_r.

For the planar setup, the fluid is modeled as three equivalent masses: two lateral masses (m_1 and m_2) and one central mass (m_3). Their vertical and horizontal positions ($z_{01}, z_{02}, z_{03}, x_{m1}, x_{m2}$) are determined according to the selected geometry. For rectangular or cylindrical tanks, direct geometric relations are used, while for oblate tanks an interpolation based on pre-defined data is applied to determine the characteristic heights ($a_{\text{mg}}, b_{\text{mg}}$) as a function of the fill level based on the results in [19][9].

The model also computes the horizontal (k_{3x}) and vertical (k_{3z}) stiffness of the central meniscus, estimated respectively from the apparent gravitational force ($g_{\text{eff}} = \|\mathbf{a}_B\|$) and from a characteristic fluid parameter. The horizontal damping coefficient c_{3x} is assumed for the case studied but the results from Section 3.5.1 should be applied for each shape by the classical relation $c = 2\zeta\sqrt{k\,m}$.

Regarding the drop mode, no influence on its setup comes from tank shape except from the length of the springs implicitly derived.

Finally, dimensions and shape of the tank influence strongly the whole computation of static inertia executed in each mode. For Mode 1 the inertia is computed a simple solid equivalent for each partially filled tank shape. For Mode 2, inertia is included in the initial parameter computation proceeding with a base component of the fluid non-implied in the meniscus (representative of Mode 1 inertia), then adding to it the contribution of the lateral and central masses.

In particular, the static inertia of a partially filled tank can be estimated by treating the fluid as a rigid body. For rectangular and cylindrical tanks, the fluid is approximated as a block of height equal to the fill level. The inertia about a horizontal axis is then computed using standard formulas:

$$I_{\text{rect}} = m_{\text{fluid}}\frac{h^2}{3} + m_{\text{fluid}}\frac{B^2}{12}, \tag{5.1}$$

$$I_{\text{cyl}} = m_{\text{fluid}}\frac{h^2}{3} + m_{\text{fluid}}\frac{R^2}{4}, \tag{5.2}$$

where h is the fluid height, B the rectangular width, R the cylinder radius, and m_{fluid} the fluid mass.

For spherical or oblate tanks, the fluid distribution is more complex. The inertia

can be approximated by decomposing the fluid into horizontal disks corresponding to the relative height cross-sections, by using hemispherical/ellipsoidal approximations or simply by using rounded rectangular container values instead. These approaches provide a practical estimate of the I_{base}, representing the bulk fluid mass, which is valid for both high-g and low-g static conditions.

In low-gravity conditions, it is needed to consider the fluid rise along the walls that forms a meniscus. In the model, the contribution of the fluid rise along the wall is computed by the parallel axes theorem applied to the discrete lateral and central masses m_1, m_2, m_3 located at positions (x_i, z_i):

$$I_{\text{meniscus}} = m_1(x_1^2 + z_1^2) + m_2(x_2^2 + z_2^2) + m_3(x_3^2 + z_3^2). \tag{5.3}$$

The total inertia when considering the planar motion is computed as:

$$I_{\text{total}} = I_{\text{base}} + I_{\text{meniscus}}, \tag{5.4}$$

Some additional investigations can be done also via CFD for the accurate inertia computation. However, the presented framework is present in the model to contribute to a complete analysis.

5.3 Environment Inputs

To run the simulation in planar setup the acceleration and rotational behavior of the tank can be shaped to represent different mission phases. These are designed in the file `generate_inputs` that shapes the time-series vector for acceleration, rotation and angular acceleration vector for various cases. `launch` represents launch conditions by high magnitude [multiple g_0 m/s^2] acceleration varying in axes components due to a slew rotation. This aspect is particularly interesting for the validation of the body frame component when visualizing the high-g pendulum position during the re-orientation. `orbit` takes typical angular rotations and low thrust by typical maneuvers in orbit. In this case the magnitude of the acceleration is low [$g_0 \cdot 10^{-1}$m/s^2] and the representative mode can vary for different tank dimensions and fluid densities, potentially being already a representation of the intermediate Bond number range. Also inputs from typical Comet-I orbit maneuver are included. `idle` represent no

maneuvering spacecraft, which falls into low-g conditions. Different orbit levels of effective gravitational accelerations are modeled to analyse respective behavior of various sizes of tank. Other cases as `separation` try to model short impulses and characteristic behaviors. If the 3D model is considered the inputs that need to be shaped are forces and torques which govern the dynamics via generalised forces in the respective EOM derived from the Lagrangian. These are the external contributions to the motions when the tank motion is described by all degrees of freedom.

5.4 Switching Condition

In the computational implementation of the model, the switching condition has been at first model as sharp switch between stable modes. However, it has been considered valuable to design a more physical and gradual transition from a stable mode to the other. A approximate system has been written but it does not result fully integrated with the functional model. In particular the model considers an intermediate range $0.1 < Bo < 10$ where the two extremes are related by a connecting function, such that the intermediate dynamics of the fluid is defined as influenced by both modes. As mentioned in previous sections, the transition from low-g dominance to high-g dominance can be considered logarithmic. For this reason, the two ranges can be connected by a logarithmic function of Bo. The relative weights of these two mode are:

$$w_1 = max\left(0, \left(min(\frac{logBo - log0.1}{log10 - log0.1}, 1)\right)\right)$$
$$w_2 = 1 - w1$$

This represents a stable intermediate configuration in a range where any dominance can be established by analytical or experimental results reviewed. When the drop is activated, the weight of its mode is based on the transition time passed as

$$w_3 = \left(1 - \frac{t}{t_s}\right)$$

Then all the computed weights are normalised to have a total weight of 1. In such way mass stays constant and defined from function parameters, and does not create unjustified extra energy of the system. The same attention should be put

to other variables computed in the dynamics. For the output of evolving DOF overlapping some fine averaging could be necessary on the generalised coordinate and its derivatives.

From this derivation, the total configurations are: dominance of Mode 1 (stable), dominance of Mode 2 (stable), intermediate range with constant Bo value (stable), transition with drop activated (unstable, lasting t_s). The modes' weights are computed in the Bond number block and all the dynamics subsystem are run in parallel. The respective outputs are weighted after the dynamics computation to output forces, torques and MOI. This part of the implementation in the model is not completed and needs to be reviewed and made functional on this base.

Naturally, such switching behavior is thought to output smoother functions and not to represent modes as separated fluid motion. However it is only a draft on which to elaborate when validation results are available.

The model can be run in a planar setup with a sharp-switch condition, providing outputs for position and forces. However, it requires further refinement to incorporate all the theoretically derived parameters and three-dimensional dynamics, which the author could not include within the time-frame of the thesis. Priority was given to establishing the functions and equations together with the Simulink model framework. As an initial step of validation, the input parameters can be adjusted to simulate experimental setups reported in the literature, allowing comparison of the model's force outputs with commonly measured experimental values. However, identifying representative experiments for all required cases may not be trivial. In general, for preliminary results under low-g and high-g conditions, the oscillation frequencies and position vectors have been compared to analytical values and realistic maneuver scenarios, showing satisfactory agreement. Due to the complexity of the setup, validation of the equations and functions requires ad hoc experimental setups, using pressure sensors or optical devices to track oscillatory behavior, or computational fluid dynamics (CFD) simulations to fine-tune and correct parameters based on analytical studies.

Chapter 6

Conclusions

The aim of this thesis was to investigate the phenomenon of sloshing, both from the perspective of its physical behavior and its influence on spacecraft maneuvering and stability. Sloshing is of particular concern in the AOCS domain because the movement of fluid can shift the spacecraft's center of mass and generate forces and torques that could destabilise the structure or the efficiency of AOCS hardware itself. A review of the existing literature revealed that a common approach to address sloshing is through CFD, which, although accurate, is computationally expensive and less practical for simulations.

Recognising these limitations led to a key objective of this work: the development of a sloshing model that preserves physical accuracy while remaining computationally efficient for use in AOCS simulations. The importance of such modeling lies in the fact that propellant mass can account for a substantial portion of a spacecraft's total mass. Therefore, fluid motion can strongly couple with spacecraft dynamics. If uncontrolled or unaccounted for, this coupling can compromise stability, control and performance. In particular, resonances between fluid oscillations and spacecraft structural or control frequencies must be avoided to prevent detrimental amplification effects.

To address these matters, studies spanning from the 1960s to the present day were reviewed, and data were collected from experiments and analyses on different tank geometries and operating conditions. These datasets were organised and merged to establish parameters for mechanical equivalents across different mission stages. Combining results from diverse experimental setups was especially valuable in addressing variations in tank geometry, as very few experiments have examined the

same behavior across all common tank shapes. Based on these data, new models were developed and analysed in greater depth.

A key contribution of this thesis is the development of fully coupled equations for three different mechanical-equivalent models of sloshing, thereby extending their applicability to a wider range of spacecraft configurations. Different phases of the mission were mapped to representative modes, each with derived governing equations. A switching-mode system was implemented, and a Simulink model was created for integration into an AOCS simulator. Inputs and outputs were selected to match OHB's AOCS dynamic model, ensuring compatibility with industrial simulation frameworks. The ability to switch between distinct sloshing models during a mission is a novel feature of this work, enabling accurate representation of varying fluid behaviors under different operational regimes.

The model structure allows for the implementation of multiple oscillating subsystems, which is particularly advantageous for modular AOCS setups. It is designed to operate under any thrusting or maneuvering condition, tank geometry, or propellant type, making it versatile and reusable across a broad range of spacecraft projects.

In particular the following modes have been shaped, and combined in transient states, for the analysis: Mode 1 describes high magnitude effective acceleration applied to the tank. The fluids accumulates on the tank in the direction of the effective acceleration and undergoes to potentially high amplitude oscillations: Mode 2 describes the behavior of the fluid in microgravity. The fluid configures in the tank in different way, modifying the mass distribution of the the tank, while the oscillation are slower and of smaller amplitudes. Mode 3 is a transitory state describing part of the fluid concentrating in a drop, free moving in the tank.

6.1 Discussion

The developed models preserve the key parameters as oscillation frequency and main masses motion consistent with the physical fluid motion. Nonetheless, to produce and derive governing equation which were both analytically and intuitively accessible and tunable some simplifying assumptions were required.

- Only the first sloshing mode was considered relevant and modeled for all three representations.

- Some parameters still rely on linear approximations even for curved tanks, particularly in Mode 2 for the skidding of lateral masses.
- In Mode 2 and Mode 3, the discrete distributions of masses and springs were intended as initial approximations of continuous mass and force distributions. These could be refined by using annular rings for the raised fluid mass or by increasing the number of springs to better capture the spherical elastic response.

A further challenge was the lack of comprehensive datasets covering all combinations of tank shape, fill ratio, and gravity level for the oscillation characteristics of the capillarity-dominated case. This limitation led to certain parameters being estimated from incomplete information, and these should be revisited through targeted simulations or experiments. Finally, as discussed at the end of the previous section, the application of the actual Simulink model are, at the moment, limited to a planar case. All the theory needed to set up the equivalent 3D case are all presented in these thesis, basically focusing only on the different EOM derived with multiple degrees of freedom. The set up of the switching logic can be kept the same.

6.2 Future Work

The present model is fully functional and integrated into Simulink for most components, with some equations already computed and ready for block implementation. For the next steps of this project, it is important to validate the output results of this thesis work and proceed with the integration of the model with the complete AOCS framework. In particular:

- Experimental validation: testing selected tank geometries under controlled conditions to verify oscillation frequencies, damping behavior, and coupling effects with spacecraft motion. While challenging in an industrial environment, such experiments would provide high-confidence validation for the simplified mechanical-equivalent approach.
- CFD-based validation: running CFD simulations for different tank geometries, fill levels, and acceleration/rotation profiles to generate reference data. Extracting key parameters (forces, interface shape, oscillating mass, total system energy) for comparison with the mechanical-equivalent outputs. These would be then used to tune or modify parameters shaped in Mode 2 and Mode 3, and in

curved tanks.

- Controller design and integration: using the present model as plant for the designing of feedback and feedforward control laws. These could be tested to damp the disturbances of sloshing actively, while being integrated within the AOCS simulation environment to assess its impact on pointing stability and maneuver accuracy.
- Switching system refinement: the switching system, implemented both in discrete and continuous form, is generalised and uses representative but simplified thresholds, especially for Mode 1 and Mode 2 dominance. These thresholds should be tuned based on monitored parameters from simulation or fight-data when available. This would ensure higher accuracy and reliability of the model in different mission phases.
- Non-linearised model -physical constraints: the physical constraint of the tank geometry and components should be analysed with regards to the impact on the equivalent model dynamics. Analysis on the effects should also be performed to see the actual impact of possibly incoherent geometry on the actual dynamics results.
- Swirling and spinning: more work should be done to define the lever of relevance of the fluid swirling or spinning during flight and in case to add modes representing these conditions. As for current situation, the spinning has been considered only along the longitudinal axis in a separate mode not fully wired to the rest of the model.

In conclusion, this thesis delivers a flexible, reusable, and broadly applicable sloshing model that combines physical accuracy with computational efficiency, making it suitable for a wide range of spacecraft configurations and mission profiles. Before advancing to control design, the model should be thoroughly verified through targeted experiments and high-fidelity CFD simulations to ensure its predictive accuracy under different operating conditions. Once validated, the natural next step is the development of a dedicated controller capable of actively mitigating sloshing effects, thereby enhancing the stability, precision, and reliability of future spacecraft AOCS systems.

References

[1] Abramson, H.N. “The Dynamic Behavior of Liquids in Moving Containers.” In: *NASA SP-106* (1966).

[2] Alazard, Daniel, Cumer, Christelle, and Tantawi, Khalid. “Linear dynamic modeling of spacecraft with various flexible appendages and on-board angular momentums”. In: *7th International ESA Conference on Guidance, Navigation & Control Systems*. Vol. 1. 2008, pp. 1–14.

[3] Bourdelle, Anthony, Biannic, Jean-Marc, Laurent, Burlion, Evain, Hélène, Pittet, Christelle, and Moreno, Sabine. “Modeling and control of propellant slosh dynamics in observation spacecraft with actuators saturations”. In: *EUCASS 2019*. 2019.

[4] Collicott, Steven. “Capillary Fluid Physics in Zero-Gravity”. In: *41st AIAA Fluid Dynamics Conference and Exhibit*. 2011, p. 4046.

[5] Dalmon, Alexis, Lepilliez, Mathieu, Tanguy, Sébastien, Pedrono, Annaig, Busset, Barbara, Bavestrello, Henri, and Mignot, Jean. “Direct numerical simulation of a bubble motion in a spherical tank under external forces and microgravity conditions”. In: *Journal of Fluid Mechanics* 849 (2018), pp. 467–497.

[6] De Gennes, Pierre-Gilles, Brochard-Wyart, Françoise, and Quéré, David. *Capillarity and wetting phenomena: drops, bubbles, pearls, waves*. Springer Science & Business Media, 2003.

[7] Dodge,
Franklin T. “Studies of propellant sloshing under low-gravity conditions”. In: *NASA Report contract NAS8-20290* (1970).

[8] Dodge, Franklin T et al. “The new” dynamic behavior of liquids in moving containers””. In: (2000).

[9] Dodge, Franklin T and Garza, Luis R. “Simulated low-gravity sloshing in spherical, ellipsoidal, and cylindrical tanks”. In: *Journal of Spacecraft and Rockets* 7.2 (1970), pp. 204–206.

[10] Dodge, Franklin T, Green, Steven T, and Kana, Daniel D. *Fluid management technology: liquid slosh dynamics and control*. Tech. rep. 1991.

[11] Egry, Ivan, Giffard, H, and Schneider, S. “The oscillating drop technique revisited”. In: *Measurement science and technology* 16.2 (2005), p. 426.

[12] Hahn, Manuel, Adami, Stefan, and Förstner, Roger. “Computational modeling of nonlinear propellant sloshing for spacecraft AOCS applications”. In: *CEAS Space Journal* 10.3 (2018), pp. 441–451.

[13] Hart, Samuel, Lightsey, E Glenn, and Romero-Calvo, Alvaro. “CAPILLARY AND ELECTROMAGNETIC SMALLSAT PROPELLANT POSITIONING”. In: ().

[14] Ibrahim, Raouf A, Pilipchuk, Valery N, and Ikeda, Takashi. “Recent advances in liquid sloshing dynamics”. In: (2001).

[15] Ibrahim, Raouf A. “Equivalent mechanical models”. In: *Liquid Sloshing Dynamics: Theory and Applications*. Cambridge University Press, 2005, pp. 296–337.

[16] Kana, Daniel D and Dodge, Franklin T. *Study of liquid slosh in the tracking and data relay satellite hydrazine tanks*. Tech. rep. 1981.

[17] Landau, Lev Davidovich and Lifshitz, Evgenii Mikhailovich. *Course of theoretical physics*. Elsevier, 2013.

[18] Li, Ji-Cheng, Lin, Hai, Li, Kai, Zhao, Jian-Fu, and Hu, Wen-Rui. “Liquid sloshing in partially filled capsule storage tank undergoing gravity reduction to low/micro-gravity condition”. In: *Microgravity Science and Technology* 32.4 (2020), pp. 587–596.

[19] Luppes, Roel, Helder, Joop A, and Veldman, Arthur EP. “The numerical simulation of liquid sloshing in microgravity”. In: *Computational Fluid Dynamics 2006: Proceedings of the Fourth International Conference on Computational Fluid Dynamics, ICCFD, Ghent, Belgium, 10-14 July 2006*. Springer. 2009, pp. 607–612.

[20] Space Telescope Science Institute. *JWST Pointing Accuracy*. Accessed: 2025-08-13. 2023. URL: https://jwst-docs.stsci.edu/jwst-observatory-characteristics-and-performance/jwst-pointing-performance/jwst-pointing-accuracy.

[21] Winkler, Stefan, Wiedermann, Georg, and Gockel, Wilhelm. "High-Accuracy On-Board Attitude Estimation for the GMES Sentinel-2 Satellite: Concept, Design, and First Results". In: *AIAA Guidance, Navigation and Control Conference and Exhibit*. DOI: 10.2514/6.2008-7482. eprint: https://arc.aiaa.org/doi/pdf/10.2514/6.2008-7482. URL: https://arc.aiaa.org/doi/abs/10.2514/6.2008-7482.

[22] Yang, HQ and Peugeot, John. "Propellant sloshing parameter extraction from computational-fluid-dynamics analysis". In: *Journal of Spacecraft and Rockets* 51.3 (2014), pp. 908–916.